AFRL-AFOSR-VA-TR-2023-0083

Far-from-Equilibrium Structures and Processes using Electromagnetic Fields: Non-Thermal Effects

Jayan, B.Reeja
CARNEGIE MELLON UNIVERSITY
5000 FORBES AVE
PITTSBURGH, PA, 15213
USA

10/19/2022
Final Technical Report

Air Force Research Laboratory
Air Force Office of Scientific Research
Arlington, Virginia 22203
Air Force Materiel Command

REPORT DOCUMENTATION PAGE

PLEASE DO NOT RETURN YOUR FORM TO THE ABOVE ORGANIZATION.

1. REPORT DATE	2. REPORT TYPE	3. DATES COVERED	
		START DATE	END DATE
20221019	Final	20170201	20200131

4. TITLE AND SUBTITLE
Far-from-Equilibrium Structures and Processes using Electromagnetic Fields: Non-Thermal Effects

5a. CONTRACT NUMBER	5b. GRANT NUMBER	5c. PROGRAM ELEMENT NUMBER
	FA9550-17-1-0120	61102F
5d. PROJECT NUMBER	**5e. TASK NUMBER**	**5f. WORK UNIT NUMBER**

6. AUTHOR(S)
B.Reeja Jayan

7. PERFORMING ORGANIZATION NAME(S) AND ADDRESS(ES)
CARNEGIE MELLON UNIVERSITY
5000 FORBES AVE
PITTSBURGH, PA 15213
USA

8. PERFORMING ORGANIZATION REPORT NUMBER

9. SPONSORING/MONITORING AGENCY NAME(S) AND ADDRESS(ES)	10. SPONSOR/MONITOR'S ACRONYM(S)	11. SPONSOR/MONITOR'S REPORT NUMBER(S)
Air Force Office of Scientific Research 875 N. Randolph St. Room 3112 Arlington, VA 22203	AFRL/AFOSR RTB1	AFRL-AFOSR-VA-TR-2023-0083

12. DISTRIBUTION/AVAILABILITY STATEMENT
A Distribution Unlimited: PB Public Release

13. SUPPLEMENTARY NOTES

14. ABSTRACT
This project will build a comprehensive framework for understanding how electromagnetic fields, in particular their low energy non-thermal effects, can synthesize far-from-equilibrium materials, such as mixtures of amorphous and crystalline oxides, disordered glass-like alloys, and oxide-polymer composites with tailored structures and properties. Such processes and materials have widespread appeal in Air Force relevant technologies for structurally integrated energy conversion, actuators, and sensors, information storage, optoelectronics, solid-state refrigeration. The non-thermal effects of electromagnetic fields can produce far-fromequilibrium outcomes, which cannot be achieved through conventional processing. For instance, the low temperature (~ 150 oC) crystallization of ceramic oxide (e.g., anatase TiO2) thin films by microwave radiation is a potential non-thermal effect, as conventional synthetic routes even under the same temperature profile cannot reproduce the results. The novelty of my approach to study non-thermal effects lies in using thin film growth experiments in which field interactions can be selectively localized to a desired region inside the reaction vessel (e.g. the substrate). Such experiments can systematically examine the effects of field intensity, temperatures, and reaction mechanisms at a specific point instead of in the bulk of the solution. Specifically, I will couple experimental and computational methods for temperature

15. SUBJECT TERMS

16. SECURITY CLASSIFICATION OF:			17. LIMITATION OF ABSTRACT	18. NUMBER OF PAGES
a. REPORT	b. ABSTRACT	c. THIS PAGE		
U	U	U	UU	35

19a. NAME OF RESPONSIBLE PERSON	19b. PHONE NUMBER *(Include area code)*
ALI SAYIR	426-7236

Final Report

1. Introduction: It has been observed that when materials are subjected to far-from-equilibrium conditions, such as application of an electromagnetic (EM) field, the resulting material can exhibit interesting material properties and metastable phases that are not seen when subjected to conventional thermal processes.[1, 2] However, the mechanisms behind these phenomena are not fully understood. While some have speculated that they are due to the rapid heating rates that occur during EM field application,[3] there is mounting evidence in the literature that these phenomena are caused by 'non-thermal' effects (Figure 1). Non-thermal effects are caused by a direct coupling between the field and the irradiated material,[2] which could explain events such as ceramic thin films synthesis being synthesized occurring at lower temperatures than is conventionally required.[4] In this experiment, a TiO_2 thin film was grown and crystallized using a sol-gel deposition method onto a plastic substrate (melting temperature of 250 ℃), suggesting that this process was carried out below a temperature of 250 ℃, where conventional TiO_2 thin film syntheses require 450 ℃ for film growth. This behavior cannot be explained by the concept of thermal runaway.

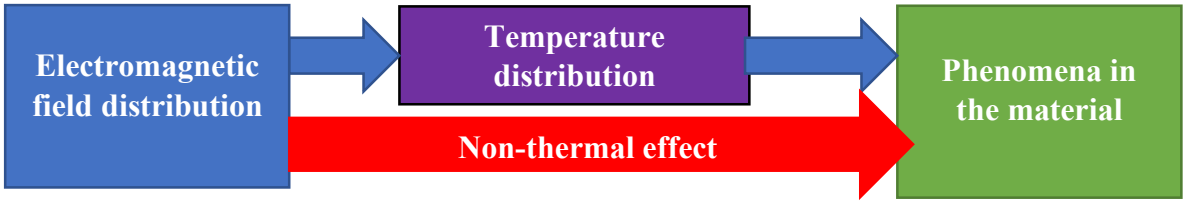

Figure 1: The schematic representation of the direct coupling between the material and EM field rather than local heating, which in turn leads to phase transformations.

Non-thermal effects may also explain why we see metastable phases and mixed amorphous-crystalline mixtures being synthesized using a similar sol-gel deposition method.[5] By introducing new variables into the conventional processing framework (e.g. intensity, frequency and duration of EM field), materials and components that will benefit the Air Force can be created and optimized, including coatings for stealth craft,[6] selective wavelength windows,[7] and anti-drone technology,[8] among others.

2. Objectives: This project aimed to find evidence of non-thermal effects when matter is subjected to EM waves, which may explain the *far-from-equilibrium* phenomena that are absent during conventional processing methods. To achieve this goal, the project is divided into the following 3 scientific objectives:

1. Measure the localized temperature induced by selective interaction between the growth substrate and the EM field. This can confirm the low-temperature nature of these reactions by yielding information about the temperature profile during processing.
2. Study mechanisms that lead to the *far-from-equilibrium* behavior that is observed. These include the polarization mechanisms that are active when matter couples with the EM field as well as the mechanisms behind the atomic structure and microstructure evolution (e.g. defect migration, Frenkel pair generation, strain-induced changes, etc.). *In-situ* monitoring of the process is required to complete this objective.
3. Synthesize *far-from-equilibrium* materials and metastable phases that are not generated during

conventional synthesis using EM fields, such as low-temperature cubic ZrO_2. A proposed method for isolating non-thermal effects from their thermal counterparts uses a split ring resonator system for EM field synthesis and processing of powders/thin films.

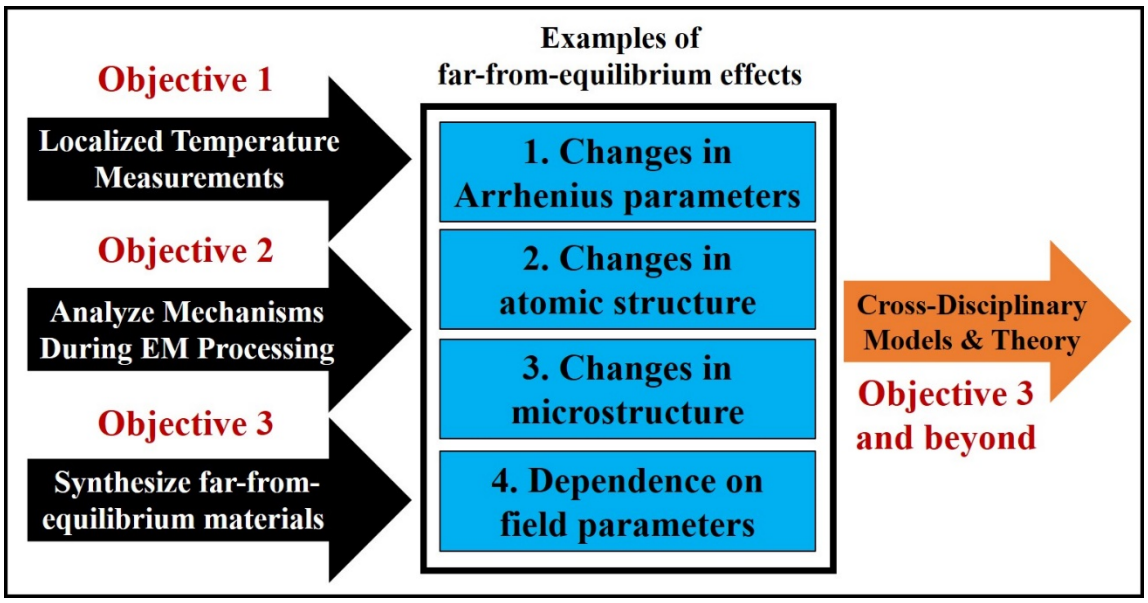

Figure 2: Overview of proposed approach to identify and investigate *far-from-equilibrium* effects.

2.1 Summary of Accomplishments: Our work merged exploratory experiments and computation with data-driven methods to define new thermodynamic foundations that better explain processes occurring away from equilibrium, like the behavior of groups of atoms under externally applied fields. Our work [see notable papers attached with report] used high-resolution synchrotron x-ray studies to demonstrate the first experimental evidence that 2.45 GHz microwave fields stabilize a different atomic structural arrangements or phase(s) in ceramics like TiO_2, compared to conventional, high temperature furnace based synthesis. Through a combination of in-situ and ex-situ characterization, as well as atomistic simulations, we show that EM fields can induce away from equilibrium phases via a defect-mediated, field-driven, non-thermal effect [see notable papers attached with report]. Our work thus lays the theoretical foundations for deploying EM fields as a new processing tool to access high temperature ceramic phases with minimal thermal input, allowing us to explore regions of phase space, microstructures, and properties not accessible via conventional synthesis routes. ***Figure 15 is the most important finding of this project: Low energy microwave fields can shift atoms out of their lattice sites, creating structural disorder.***

PhD Thesis: Nathan Nakamura (*Defended on April 30, 2020***)**
Title: Experimental Evidence for the Effects of Electromagnetic Fields on Atomic Structure
Department of Mechanical Engineering, Carnegie Mellon University.
*Will start NRC Postdoctoral Position at NIST, Boulder, Colorado in Fall 2020.

Awards for PhD student Nathan Nakamura: Material Research Society (MRS) Fall 2018 Graduate Student Award - Silver Medal, National Defense Science and Engineering (NDSEG) Fellowship 2017, CMU Mechanical Engineering Milton Shaw PhD Research Award 2017, CMU

Mechanical Engineering Nam Pyo and Young Suh Fellowship 2017, CMU Milton Shaw PhD Student Travel Award 2017.

PhD Thesis: Maxwell Telmer (expected to graduate in Fall 2021)
Title: Role of Frequency Dependent Polarization Effects in Field-Matter Coupling
Department of Mechanical Engineering, Carnegie Mellon University.

Awards for PhD student Maxwell Telmer: Air Force Research Laboratory (AFRL) Summer Scholarship 2018 - 2020, Best Poster in Symposium - Materials Research Society (MRS) Fall 2018 Meeting, CMU Summer Undergraduate Research Fellowship (SURF) Award 2016, CMU Small Undergraduate Research Grant (SURG) Award 2017.

Awards for PI B. Reeja Jayan: CMU Engineering Dean's Early Career Fellow (one of two winners in 2020)**,** 54th Annual Keynote Speaker, International Microwave Power Institute (IMPI, 2020)**,** Invited attendee at 2020 Roundtable on Biomedical Engineering Materials and Applications (BEMA), National Academy of Engineering (NAE), U.S. Department of Energy (DOE) Faculty Research Program Participant - National Energy Technology Laboratory (NETL), ORISE/ORAU 2020, Faculty Fellow, Scott Institute for Energy Innovation (2019), George Tallman Ladd Research Award (2019)**,** National Science Foundation (NSF) CAREER Award (2018, Army Research Office (ARO) Young Investigator Award (2017, Pittsburgh Magazine 40 Under 40 Award (2017), The Incline Who's Next: Technology Award – 18 People Transforming Pittsburgh (2017)**,** Donald L. and Rhonda Struminger Faculty Fellow in Mechanical Engineering (2017), Berkman Faculty Development Fund (2017).

*Promoted to Associate Professor of Mechanical Engineering at Carnegie Mellon University; effective 1 July, 2020

List of Peer Reviewed Publications & Selected Presentations from YIP project

1. N. Nakamura, B. Reeja-Jayan, "Defect-Mediated Phase Transitions under Electromagnetic Excitation", *submitted*, 2020.
2. N. Nakamura, L. Su, J. Bai, S. Ghose, and B. Reeja-Jayan, "*In Situ* synchrotron pair distribution function analysis to monitor synthetic pathways under electromagnetic excitation", *Journal of Materials Chemistry A*, 2020. ***2020 Emerging Investigators Themed Issue.***
3. N. Nakamura, B. Reeja-Jayan, "Synchrotron x-ray characterization of materials synthesized under microwave irradiation", *Journal of Materials Research*, 2019, 34, 194-205.
4. N. Nakamura, M. W. Terban, S. J. L. Billinge, B. Reeja-Jayan, "Unlocking the structure of mixed amorphous-crystalline ceramic oxide films synthesized under low temperature electromagnetic excitation", *Journal of Materials Chemistry A*, 2017, 5, 18434-18441.
5. S. K. Jha, X.L. Phuah, J. Luo, C.P. Grigoropoulos, H. Wang, E. García, B. Reeja-Jayan, "The Effects of External Fields in Ceramic Sintering," *Journal of the American Ceramic Society*, 102, 5-31 (2019). ***Article was selected as front cover of journal for January 2019.***
6. Telmer, M. R.; Hilario, M. S.; Hoff, B. W., Lanagan, M. T.; Reeja-Jayan, B. "Anisotropy of W-band complex permittivity in Al_2O_3" *Journal of Physics: Condensed Matter* 2019, 31, 225702

7. B. Reeja Jayan, "Why Microwave-Heating is More than Just Heating," *Invited Keynote Speaker*, 54th Annual Microwave Power Symposium, **International Microwave Power Institute (IMPI)**, 15 June 2020.
8. B. Reeja Jayan, "Engineering Far-From-Equilibrium Materials Using Electromagnetic Fields," *Invited Speaker*, Basic Research Forum, **US Department of Defense**, 13 Feb 2020.
9. N. Nakamura, E. Culbertson, S. J. L. Billinge, B. Reeja Jayan, "X-ray Synchrotron Investigation of ZrO_2 Phase Formation under Electromagnetic Excitation", *Materials Research Society (MRS) Fall Meeting 2019*, Boston, USA, Dec. 1-6.
10. N. Nakamura, E. Culbertson, H. Wang, H. Wang, C. S. Hellberg, S. J. L. Billinge, B. Reeja Jayan, "The Role of Defects in Microwave-Assisted Synthesis of Cubic ZrO_2", *Electric Field Enhanced Processing of Advanced Materials II: Complexities and Opportunities 2019*, Tomar, Portugal, March 10-15.
11. B. Reeja Jayan, "Low Temperature Ceramic Crystallization via Electromagnetic Field Interactions at Interfaces", *Invited talk* in **Rustum Roy Symposium, Materials Science & Technology Conference & Exhibition (MS&T18)**, Columbus, USA, 14 Oct-18 Oct 2018.
12. B. Reeja Jayan, "Low Temperature Ceramic Crystallization via Electromagnetic Field Interactions at Interfaces" *Invited Speaker*, **Gordon Research Conference on Solid State Studies in Ceramics**, Mount Holyoke College, 12-17 August 2018.
13. B. Reeja Jayan, "Electromagnetic Fields Coupling to Matter. How can we distinguish thermal and field effects?," *Invited Seminar* at **US Naval Research Laboratory (NRL)**, Alexandria, Virginia, 10 July 2018.
14. N. Nakamura, E. Culbertson, S. J. L. Billinge, B. Reeja Jayan, "Low-Temperature Phase Transitions in Ceramic Oxides via Electromagnetic Field Exposure", *Materials Research Society (MRS) Fall Meeting 2018, Boston*, USA, Nov. 25-30.
    - **Award: MRS Graduate Student Award - Silver**
15. N. Nakamura, E. Culbertson, S. J. L. Billinge, B. Reeja Jayan, "Electromagnetic Field Effects on Atomic Structure in Ceramic Oxide Thin Films", *Materials Science and Technology (MS&T) Meeting 2018*, Columbus, USA, Oct. 14-18.
16. N. Nakamura, E. Culbertson, H. Wang, H. Wang, S. J. L. Billinge, B. Reeja Jayan, "Electromagnetic Field Effects on Atomic Structure and Phase Transitions in Ceramic Oxide Thin Films", *Gordon Research Conference (GRC) – Solid State Studies in Ceramics 2018*, South Hadley, USA, Aug. 12-17.
17. N. Nakamura, M.W. Terban, S. J. L. Billinge, B. Reeja-Jayan, "Evolution of Distinct Phase Composition in Ceramic Thin Films Grown under Electromagnetic Excitation", *Materials Science and Technology (MS&T) Meeting 2017*, Pittsburgh, USA, Oct. 8-12.
18. N. Nakamura, M. W. Terban, S. J. L. Billinge, B. Reeja Jayan, "Unlocking the structure of mixed amorphous-crystalline ceramic oxide thin films synthesized under electromagnetic excitation", *The 75th Annual Pittsburgh Diffraction Conference*, October 2017
19. N. Nakamura, B. Reeja Jayan, "Unlocking the structure of mixed amorphous-crystalline ceramic oxide thin films synthesized under electromagnetic excitation", *Air Force Office of Scientific Research (AFOSR) Student Research Day*, September 2017

20. Telmer, M. R.; Reeja-Jayan, B. "Characterizing the Role of Thin Film Interfaces in Field-Assisted Materials Processing" *Materials Research Society (MRS) Fall Meeting*. 2018.
    - **Award: Best poster in symposium**
21. Telmer, M. R.; Reeja-Jayan, B. "Ordering of PS & PMMA Thin Films Using Microwave Radiation (MWR)" *Workshop on Electromagnetic Effects in Materials Synthesis*. 2017.
22. N. Nakamura, M. W. Terban, S. J. L. Billinge, B. Reeja-Jayan, "Rapid, Low Temperature Synthesis of Amorphous-Crystalline Thin Films Under Electromagnetic Excitation", *Carnegie Mellon Energy Week Poster and Multimedia Presentation*, March 2017.
23. N. Nakamura, M. W. Terban, S. J. L. Billinge, B. Reeja-Jayan, "Microwave-Assisted Synthesis of Crystalline TiO_2 Thin Films", *Carnegie Mellon Bennet Conference*, March 2016.
24. N. Nakamura, M. W. Terban, S. J. L. Billinge, B. Reeja-Jayan, "Rapid, Low Temperature Synthesis of Amorphous-Crystalline Thin Films under Electromagnetic Excitation", *Carnegie Mellon Mechanical Engineering Graduate Student Research Symposium*, March 2017.
    - **Award: Best Poster**

3. <u>Detailed Description of Results of YIP project</u>: The following sections describe in detail our accomplishments summarized in the previous section. These sections follow from our published papers and manuscripts in submission. We will attach all such related journal papers and thesis to this report.

3.1 <u>Scientific Approach</u>: In this YIP project, we addressed previous limitations on studying EM field-matter coupling during materials synthesis by using novel synchrotron x-ray analysis tools and by developing instrumentation to enable *in-situ* x-ray scattering studies during EM field application.

While EM field-assisted synthesis can induce non-equilibrium phases, the mechanisms underlying how MWR influences phase stability remain elusive.[9] Two significant bottlenecks to achieving this understanding are (1) analyzing how EM fields affect local atomic structure, and (2) assessing the influence of EM fields on structure in real-time. Analyzing the local atomic structure is critical, as EM fields may create local structural distortions or promote amorphous phase formation, neither of which is detectable by studying the long-range, crystalline atomic order. To study local atomic order, we chose to utilize synchrotron x-ray pair distribution function (PDF) analysis, a total x-ray scattering technique. The term 'total scattering' refers to the inclusion of both Bragg and diffuse scattering, which enable quantitative analysis of both long and short-range atomic order. In contrast, more common techniques such as x-ray diffraction (XRD) encompass only Bragg scattering, and thus are limited to analysis of only the long-range order. The PDF is a real-space representation of atomic structure, with peak positions corresponding to interatomic distances (Fig. 3). Therefore, changes in the structure due to EM fields exposure are represented directly by change in the position, intensity, or width of the measured peaks. Additional quantitative information is obtained via a phase refinement, in which the calculated PDF from a reference structure is fit to the data. The quality of this fit is given by the goodness-of-fit, R_w, where a lower R_w indicates a higher quality fit.[10, 11]

In addition to the structural information PDF provides, it is necessary to develop instrumentation capable of monitoring EM fields in real time. Such *in-situ* tools enable the characterization of any metastable intermediate phases that may form and can provide unprecedented insight into what may be driving the low temperature crystallization and phase formation observed.

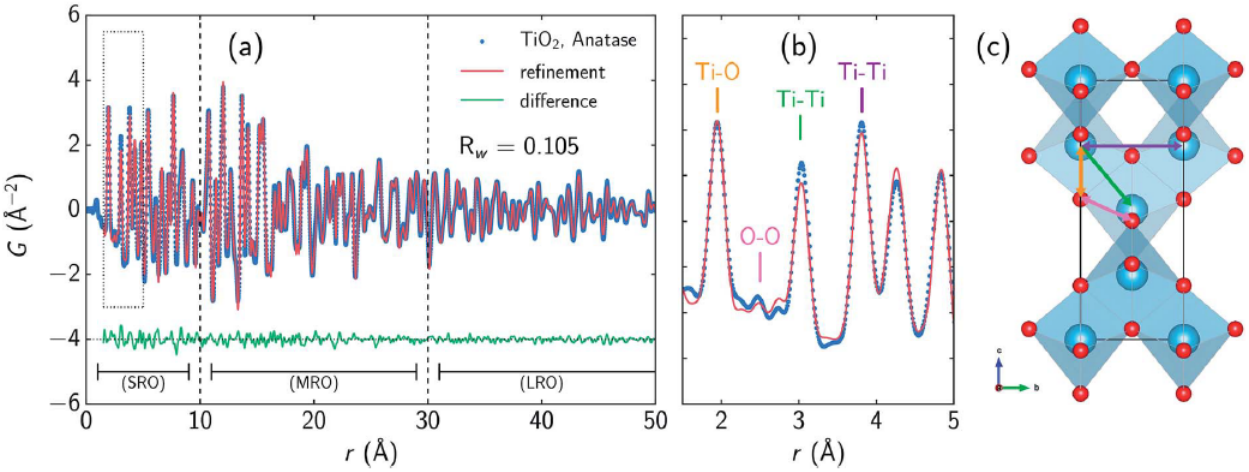

Figure 3 (a) PDF data (blue) for commercially available anatase TiO_2 powder with the simulated PDF (red) from refinement of the anatase structure. The difference is shown below offset in green. The regions for short-range (SRO), medium-range (MRO), and long-range order (LRO) are labelled. (b) Magnified view of the low-r, boxed in region from (a). Specific PDF peaks are labelled and color-coded, with the respective interatomic distance in the anatase structure shown in (c).

4. Objective 1: Measuring Localized Temperature: In our experiments, we used fiber optic (Neoptix T1) and infrared (IR) temperature probes to measure temperature by placing them inside a solution contained within the reaction vessel exposed to MWR fields. Details are discussed under section 5.2 of Objective 2, which describes our attempts to dynamically track (in-situ) reactions occurring under EM field exposure. Here we found that local solution temperatures remained low during the MWR application, allowing us to primarily attribute the structural disorder driven phase transitions to field exposure. However, we realized that a finer spatial resolution and mapping of the temperature is a more involved task, which was beyond the scope of this 3-year YIP project.

5. Objective 2: Study the mechanisms of *far-from-equilibrium* behavior

We spent most of our 3-year YIP project on attaining this scientific objective.

5.1 Seminal Experimental evidence that low energy EM fields influence atomic structure *(ex-situ data)*

Summary: We discovered the first experimental evidence that even low energy electromagnetic fields can influence atomic structural arrangements using a combination of experimental techniques aided by first-principles calculations. Our experiments use synchrotron pair distribution function (PDF) analysis and x-ray absorption spectroscopy (XAS) to quantitatively connect increases in local electric field strengths to increased local structural disorder in ceramic oxides like TiO_2 and ZrO_2. Density functional theory (DFT) calculations reveal that this local structure is

consistent with oxygen defect formation and explains the low temperature crystalline phase formation.

Description of Results: Our first experiments involved synthesizing ceramic oxide thin films via MWR-assisted synthesis and characterizing their atomic structure *ex-situ* using PDF analysis. MWR-assisted thin film synthesis was performed using an Anton Paar Monowave 300 microwave reaction system operating at 2.45 GHz. Details have been reported previously.[4, 12] A sol-gel solution based on tetrabutyl orthotitanate was used as the precursor.[13] 0.55 mm thick glass substrates coated with ~100 nm of ITO with conductivity $\sigma \sim 10^5$ S/m were purchased from Nanocs (New York, NY) and cut into ~1 cm by ~0.5 cm rectangular pieces. To provide a clean surface for TiO_2 film growth, the substrates were sonicated sequentially in Alconox (detergent) solution, deionized water, isopropyl alcohol, and acetone for 10 min each. The substrate was placed inside a glass basket suspended inside a 30 ml glass vial containing 12 ml of tetraethylene glycol (TEG) mixed with 3 ml of sol-gel precursor. TEG was used as solvent to reduce film cracking.[4] The vial was then inserted into the Monowave 300, and the solution was stirred at 650 rpm throughout the reaction to avoid hotspots.[14]

Utilizing PDF analysis, we demonstrated that TiO_2 thin films synthesized using MWR-assisted synthesis resulted in significantly more crystallization and altered local atomic order compared with furnace-grown films at identical temperatures. Furnace-grown films were synthesized at 450°C, the lowest temperature generally required to obtain crystalline anatase,[15, 16] and at both 150 and 250°C to compare growth at temperatures similar to those used in MWR-assisted synthesis. PDF refinements to the furnace grown films indicate that we achieve a crystalline anatase phase at 450°C, as expected (Fig. 4a). However, when TiO_2 is synthesized in the furnace at 150°C, we find a fully amorphous structure (Fig. 4b). This amorphous structure is found to be best defined by a brookite:anatase:rutile ratio of 80:7:13. Similarly, thin films synthesized in the furnace at 250°C were also fully amorphous.

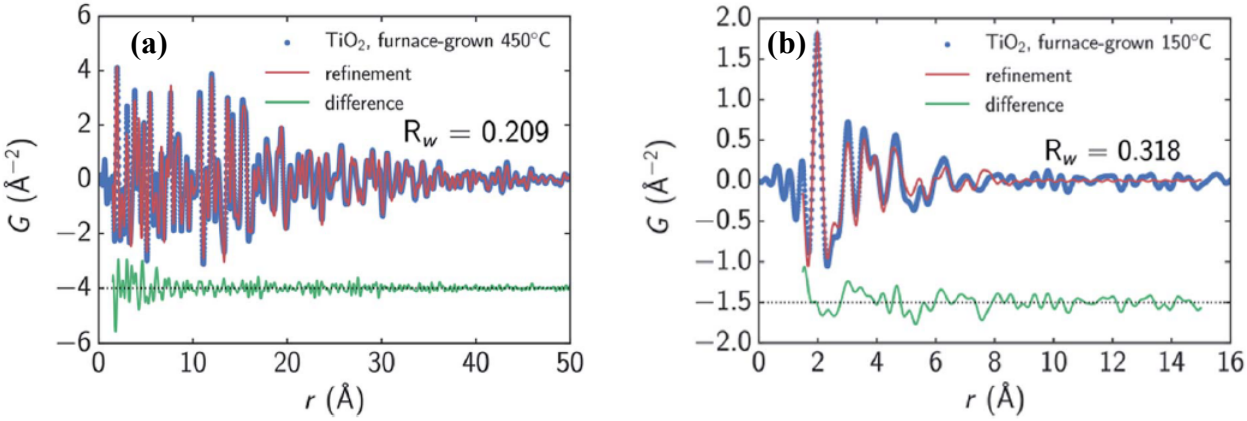

Figure 4 (a) PDF data from a TiO_2 film synthesized without EM field exposure at 450°C (blue), fit to a crystalline anatase structure (red). The difference is shown below offset in green. (b) PDF data from a TiO_2 film synthesized without EM field exposure at 150°C (blue). This film is fully amorphous, and was fit to an amorphous mixture of brookite, anatase, and rutile (red), with the difference shown in green.

The PDF results from films grown by MWR-assisted synthesis proved to be quite different from those using conventional synthesis. An MWR-grown film synthesized at 160°C, 40 W, and 60 min resulted in a mixture of nanocrystalline anatase and an amorphous component (Fig. 5). This amorphous component was fit to the same amorphous phase mixture as the furnace-grown film, with the brookit:anatase:rutile composition now coming out to 77:23:0. TiO_2 films synthesized under a variety of MWR reaction conditions consistently displayed this mixed amorphous-crystalline nature.

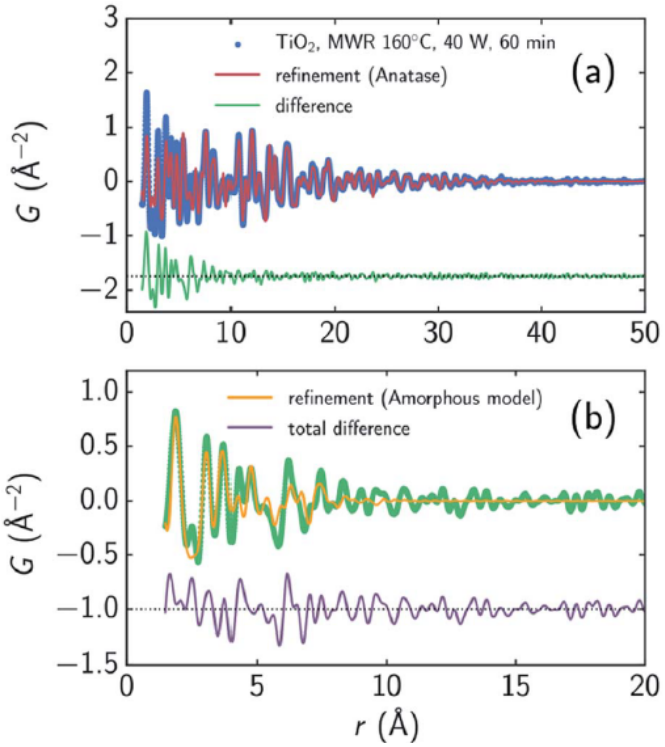

Figure 5 (a) PDF data from an MWR-grown TiO_2 film synthesized at 160°C and 40 W (blue), fit to a crystalline anatase structure (red). The difference is shown below offset in green. (b) The difference from (a), fit to an amorphous mixture of brookite, anatase, and rutile (yellow), with the difference shown in purple. The fits in (a) and (b) demonstrate the presence of a mixed amorphous crystalline structure caused by MWR exposure.

The presence of nanocrystalline anatase in MWR-grown TiO_2 represents a clear difference in the atomic structure formed by MWR-assisted synthesis in comparison with conventional furnace-based synthesis at similar temperatures. Even the SRO components form differently in each process. These structural differences suggest that the presence of MWR during synthesis influences both nucleation and growth mechanisms. This work demonstrated the power of PDF analysis for quantifying atomic structure in MWR-grown materials, and was published in 2017.[5]

To expand on the analysis of local order in TiO_2, we began exploring the origins of this local order and how it can impact phase stability in another oxide material, ZrO_2. PDF refinements to a ZrO_2 film synthesized at 225°C and 40 W reveal tetragonal ZrO_2 MRO and LRO, indicating crystalline phase formation (Fig. 6e-f). The formation of the tetragonal phase at 225°C when exposed to MWR is unexpected, as this is more than 1000°C lower than conventionally required.[17] Similar to TiO_2, furnace-grown films without EM field exposure were found to be fully amorphous, indicating MWR as a driving force for low-temperature crystallization.

Despite the LRO, the SRO is not well described by the crystalline tetragonal phase, particularly with regards to nearest neighbor distances (Fig. 6d). This suggests a local Zr-O coordination environment which differs from the tetragonal phase, potentially due to symmetry lowering relaxations. Prior work on ZrO_2 has demonstrated that oxygen point defects can induce structural changes that impact Zr-O nearest neighbor distances and the resultant phase stability,[18, 19] providing one potential source of such relaxations. To investigate how defect-based local distortions impact phase stability and compare to MWR-grown ZrO_2, first-principles Density Functional Theory (DFT) calculations were performed spanning a range of oxygen defect concentrations.

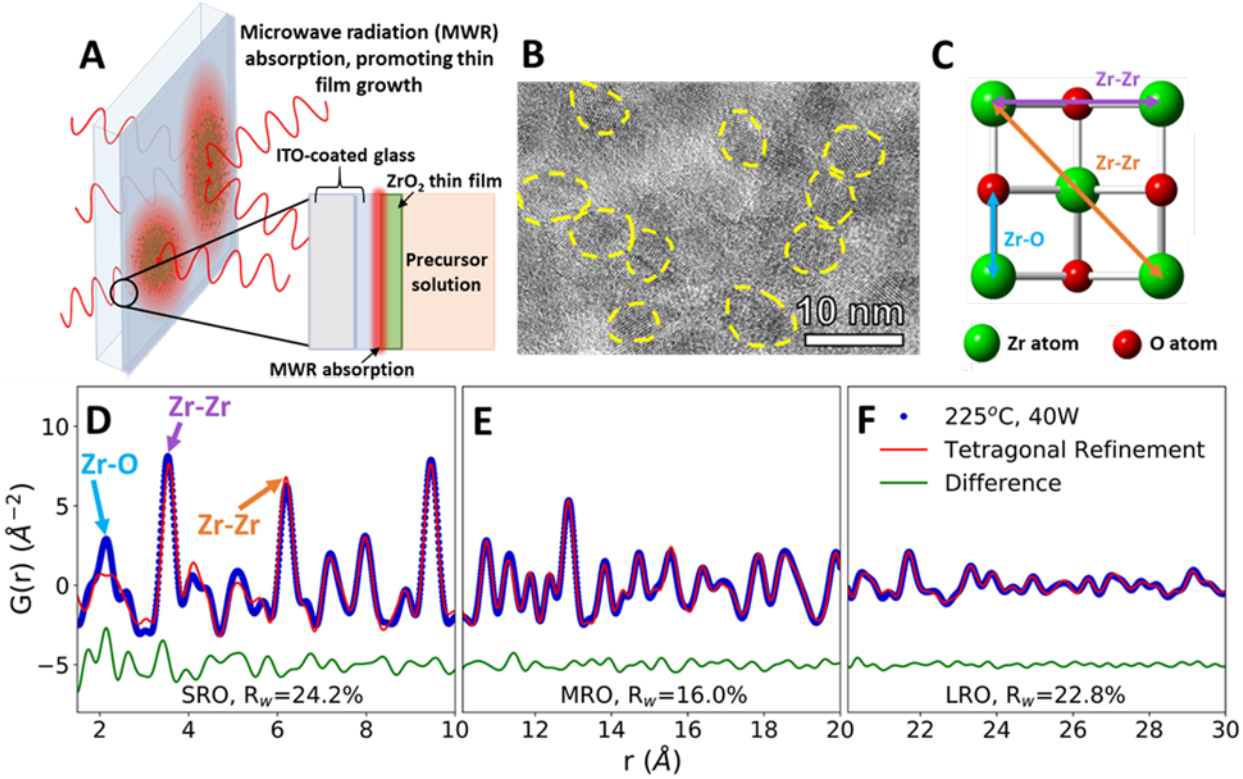

Figure 6: (a) MWR-assisted ZrO_2 thin film synthesis on an indium tin oxide (ITO)-coated glass substrate. Localized MWR absorption by the ITO layer promotes ZrO_2 nucleation and growth. (b) Transmission electron microscopy (TEM) image of the nanocrystalline MWR-grown ZrO_2 thin film (select grains outlined in yellow). (c) Atomic structure of tetragonal ZrO_2, viewed along the [001] direction. (d-f) Experimental PDF data (blue) fit to a tetragonal ZrO_2 structure (red), with the difference below in green. Zr-O and Zr-Zr nearest neighbor peaks are highlighted in (d), with their corresponding interatomic distances shown in (c). Goodness-of-fit values, R_w, are shown offset below the difference curve.

In defect-free ZrO_2, we find that the relative energies are ordered $E_{monoclinic}<E_{tetragonal}<E_{cubic}$, as expected.[20] This phase stability changes as a function of oxygen defect concentration, with a defective tetragonal phase becoming energetically favorable at a vacancy concentration of 3.2 % (Fig. 7a). The defect concentrations studied were limited by the system size of DFT calculations, yielding uncertainty regarding the exact vacancy concentration at which the defective tetragonal phase becomes favorable. However, the defective tetragonal structure shown here ($ZrO_{1.936}$) contains local atomic relaxations around vacancy sites which break the local symmetry and provides a suitable representation of oxygen vacancy-based structural distortions (Fig. 7b). This allows us to utilize the $ZrO_{1.936}$ structure as a model system to explore the possibility of defect formation in MWR-grown ZrO_2.

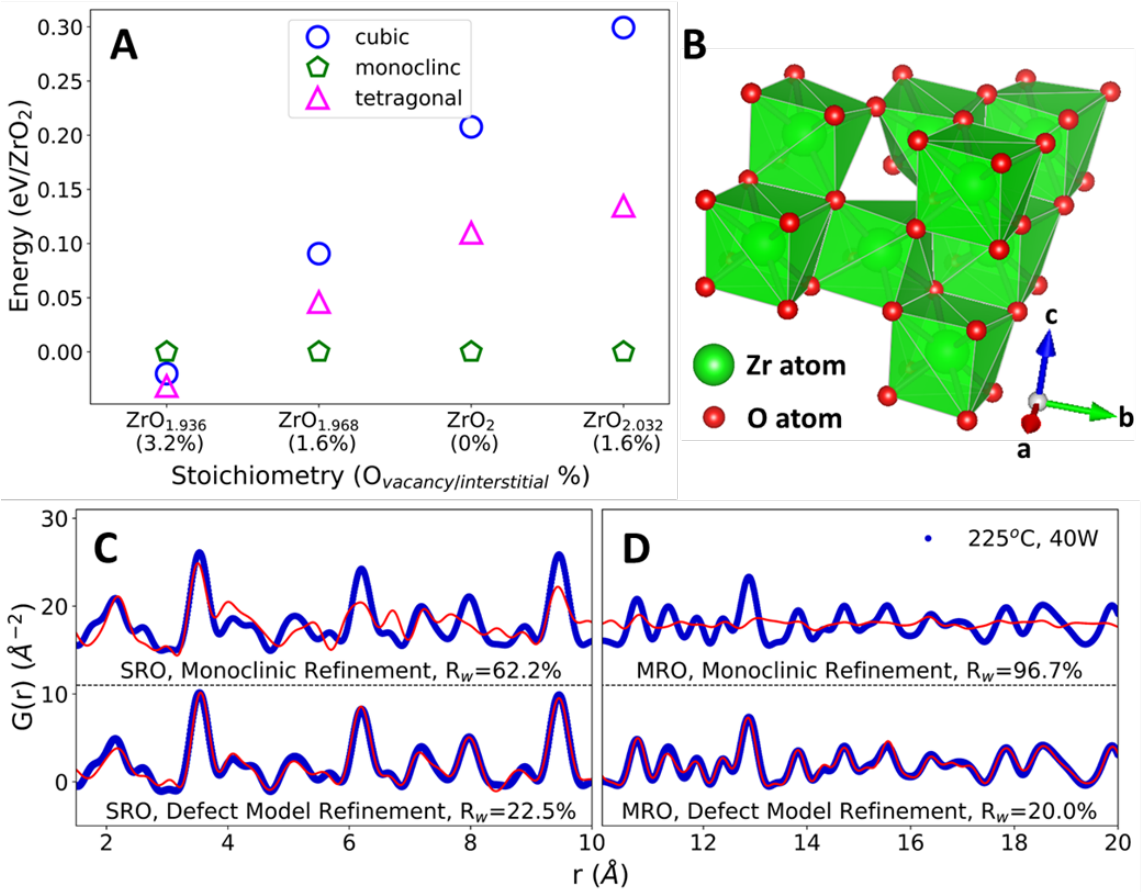

Figure 7: (a) DFT-predicted energies of ZrO_2 polymorphs with oxygen point defects, relative to the monoclinic phase. At high oxygen vacancy concentrations, a defective tetragonal structure becomes energetically favorable. (b) The DFT-predicted defective tetragonal structure. (c-d) PDF refinements of the monoclinic phase and DFT-predicted defect model (red) to MWR-grown ZrO_2 (blue). Refinements to the SRO (c) indicate that the defective phase better represents the local atomic environment than monoclinic. Comparison with the defect-free tetragonal phase in Fig. 1d indicates that the SRO is better described by oxygen-vacancy-induced structural distortions. Refinements to the MRO confirm that the local structural distortions present from defects do not break the tetragonal structure (d).

The reduced local symmetry caused by oxygen vacancies accurately represents the local atomic structure observed experimentally, as the defective model greatly improves the fit to the nearest neighbor Zr-O peak in the PDF. The lower symmetry monoclinic phase also improves the fit to nearest neighbor distances but does not describe the local order as well as the DFT-predicted defective phase. PDF fitting of the defective phase to the SRO of MWR-grown ZrO_2 results in a lower R_w value than the defect-free tetragonal or monoclinic phase, indicating that the local atomic order is better described by vacancy-induced relaxations (Fig. 7c). Overall, the defective phase improves the fit to the SRO while remaining consistent with the MRO and LRO observed experimentally, but does not improve upon the MRO and LRO from the defect-free phase. The monoclinic phase is a poor descriptor of the observed structure beyond the nearest neighbor peaks (Fig. 7d). This structural information suggests that the topology of MWR-grown ZrO_2 remains tetragonal, with EM field-assisted phase stability mediated by oxygen vacancy-induced local structural distortions. A manuscript based on this work was submitted in 2020.[5]

5.2 *In-situ* studies of EM field-assisted mechanisms

To further investigate the role of oxygen vacancies on the phase formation observed, it is necessary to characterize why they form and how they impact the phase formation process. To accomplish this, two aspects of MWR-assisted synthesis should be monitored *in-situ*: (1) the local electric field intensities at the substrate, and (2) the atomic structure during EM field exposure. This need for improved instrumentation enabling *in-situ* studies of EM field-assisted processes was outline in a review written by our group.[21] We developed novel experimental setups to accomplish both goals, based on the use of a microwave reactor designed during this proposal specifically built for *in-situ* studies.

5.2.1 Measurement of local electric field intensities: The presence of distorted local structure as a stabilizing presence in MWR-grown ZrO_2 invites investigation into the mechanisms of defect formation during MWR-assisted synthesis. Experiments utilizing an identical experimental setup and heating conditions have found that no phase formation occurs without MWR exposure, indicating that the chemical environment is not responsible for the observed effects.[22] Synthesis using a SiC vial in place of the standard borosilicate glass shields the growth solution from EM field exposure while maintaining similar heating rates,[23] and also results in no thin film growth.[4] Additionally, prior work has demonstrated that the ITO layer preferentially absorbs EM radiation and impacts the synthesis process.[4] It is suspected that electric fields on the order of 10^6 V/m, such as those present in an electric double layer, are high enough to drive ionic motion.[24, 25] This suggests that a potential driving force for oxygen vacancy formation is the presence of anomalously high field intensities at the substrate-solution interface. However, this local field strength has not previously been experimentally measured, making it difficult to link local electric fields with the resultant atomic structure.

To measure local electric field intensity, we developed a microwave cyclic voltammetry (MW-CV) technique capable of quantifying the change in electric field at the ITO layer due to MWR exposure. MW-CV represents the first experimental technique capable of monitoring local electric field intensities for EM field-assisted synthesis. When MWR is applied to the system, a positive

spike in the current is observed. Conversely, when MWR is removed, a negative spike in the current occurs (Fig. 8a). This change in current is related to a buildup of surface charge, from which the electric field intensity can be calculated. At 40 W of applied power, the increase in measured current due to MWR corresponds to an electric field on the order of 10^6 V/m, orders of magnitude higher than prior predictions of EM field-assisted processes [26]. The dependence of field intensity on interactions between MWR and the substrate material is demonstrated by an order of magnitude increase in local electric field intensity, up to 10^7 V/m, when replacing one ITO layer with a higher electrical conductivity Ti layer (Fig. 8b). Additionally, varying the H^+ concentration in the solution to alter the interaction between MWR and the solution led to an increase in the peak intensity and faster ionic motion to the ITO surface, but no significant change in the electric field intensity (Fig. 8c). Therefore, absorption of MWR by the conducting layer leads to enhanced local electric fields, which draws ions to the surface and causes an increase in current measured by MW-CV (Fig. 8d-f).

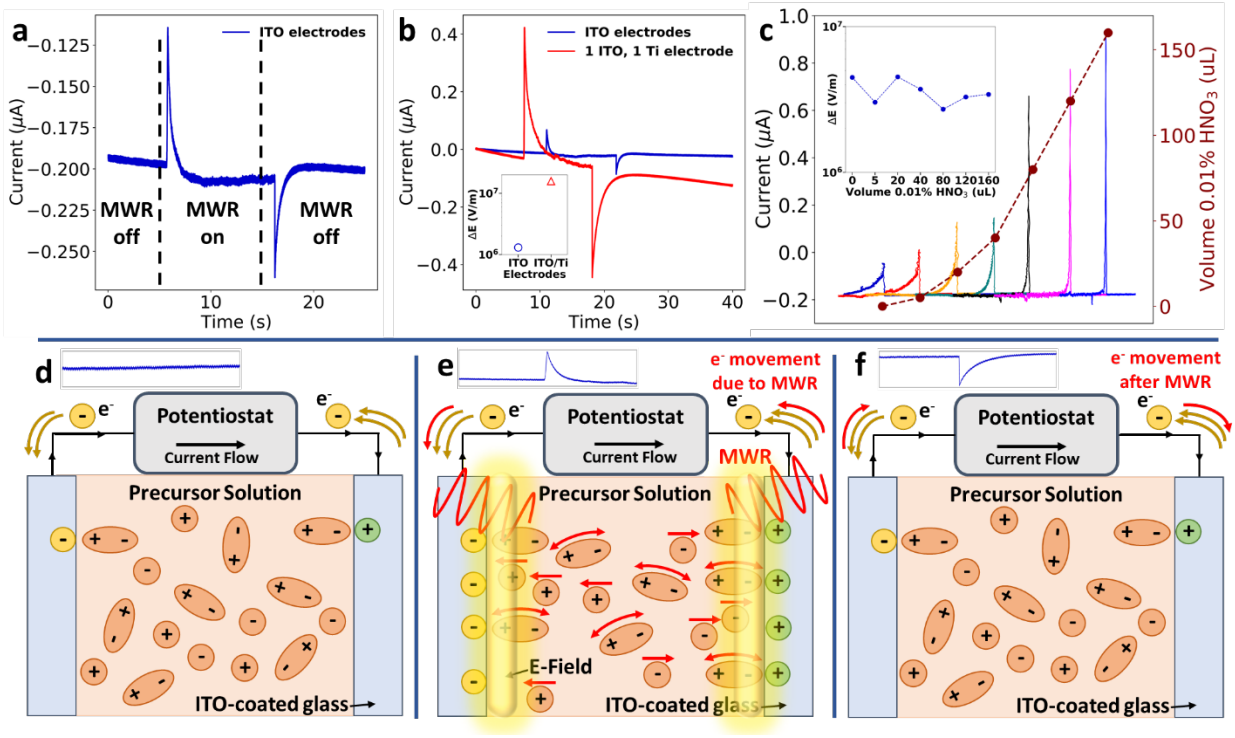

Figure 8: (a) MW-CV results indicating the change in current when the MWR is turned on (positive spike) and off (negative spike). (b) The role of the substrate on local electric field intensity. Using a higher electrical conductivity Ti layer leads to an order of magnitude increase in the electric field at the surface. (c) The role of ion concentration on local electric field intensity. Higher ion concentration increases the peak intensity, but decreases peak width, leading to no effect on the electric field at the surface. (d-f) Schematic of the mechanism of local electric field enhancement during MWR exposure. Initially, polar molecules and ions are oriented randomly in solution (d). When MWR is introduced, it is absorbed by the conducting layer and creates a large electric field at the surface. This electric field draws additional ions or molecules to the surface, leading to a spike in current to balance the additional surface charge (e). When MWR is turned off, the ions drawn to the surface release back to a random orientation, leading to a sharp negative flow in current (f).

The magnitude of the electric field intensity is found to increase with increasing MWR power levels, with higher power levels leading to higher electric field intensities (Fig. 9a). Despite the increase in field intensity, the LRO of all films remains consistent with the tetragonal phase (Fig. 9b). The SRO, however, experiences changes based on applied power. Higher electric field intensities promote more local atomic distortions, suggesting that higher power levels can induce more defects on the oxygen sub-lattice. This effect can be deduced from a noticeable change in the nearest neighbor peaks in the PDF data, leading to a decreasing quality of fit to the defective model structure (Fig. 9c). EXAFS spectra confirm this trend, with broader and less intense Zr-O peaks indicative of more structural disorder present at higher electric field intensities (Fig. 9d). This suggests that higher local electric field magnitudes can impact defect concentrations and local structural changes without breaking the crystalline LRO of a material.

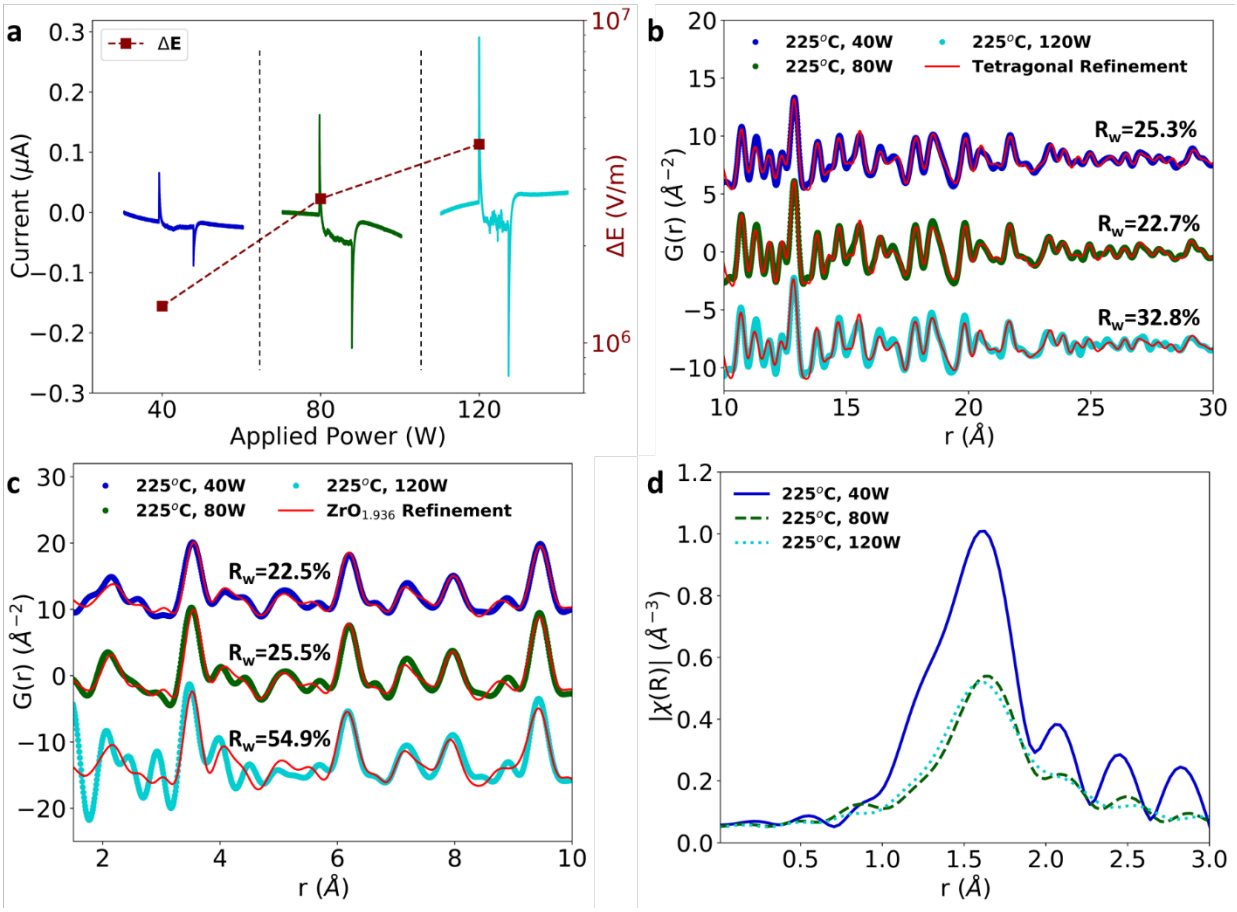

Figure 9: (a) Higher applied power leads to higher local electric fields at the ITO layer. (b) Higher power levels do not eliminate the LRO tetragonal phase, as shown by tetragonal refinements (red) to MWR-grown ZrO_2 synthesized at 225°C and 40, 80, and 120 W. (c) The SRO is impacted by the power level, as shown by refinements to the defective $ZrO_{1.936}$ phase (red). Higher power levels thus can increase local atomic disorder without sacrificing the overall tetragonal topology, suggesting that the larger electric fields present at high powers promote higher defect concentrations. (d) EXAFS spectra also indicate additional local atomic disorder with increasing MWR power, as seen by the broadening and decrease in intensity of Zr-O peaks at higher power levels.

This work demonstrates that high local electric fields can serve as a driving force for local structural changes which impact phase stability during EM field-assisted ceramic growth. With this evidence, we have obtained new insight into how synthesis and phase transitions progress under EM excitation, demonstrating that local electric field strengths are dependent on the applied power and can impact local atomic order without significantly altering the crystalline atomic structure. The characterization approach and novel MW-CV technique introduced also provides a blueprint for future studies to further analyze relationships between local electric strength, atomic structure, and phase stability in a variety of systems. Our work thus lays the practical and theoretical foundations for deploying electromagnetic fields as a synthesis tool to access new materials with minimal thermal input, allowing scientists to explore regions of phase space, microstructures, and properties not accessible via conventional chemical synthesis routes.

5.2.2 *In-situ* pair distribution function (PDF) analysis

Results:

To monitor EM field-induced structural transformations *in-situ*, an experimental setup was built enabling PDF data acquisition during MWR exposure. This equipment consists of a microwave generator capable of applying 0-1100 W power, a custom-built waveguide with inlet and outlet ports to enable x-ray exposure, and a thin-walled borosilicate tube with custom-built fittings to enable reliable sample holding inside the waveguide (Fig. 10). This experimental setup was then used to monitor SnO_2 nanoparticle synthesis during MWR exposure.

In our experiments, SnO_2 nanoparticles were synthesized from the aqueous precursor solution using both conventional and MWR-assisted synthesis. Conventional synthesis was performed by mounting a heat gun set to an output temperature of 200°C to the outside of the microwave chamber. For MWR-assisted synthesis, 2 conditions were used: (1) MWR exposure only and (2) a mixed heating condition which applies both MWR and conventional heating. Synthesis with MWR exposure only was performed by pulsing 40 W of microwave power with an on/off time of 5 seconds. The pulsed MWR deposition was used to limit pressure buildup during the reaction. Pulsing MWR exposure also results in significantly slower heating rates compared to conventional experiments. To provide a more direct comparison to conventional synthesis, it is preferable to perform MWR-assisted synthesis with a similar heating rate as the conventional experiments. This is accomplished via a mixed MWR-conventional heating condition, which creates a heating profile similar to conventional experiments. Mixed heating utilizes the heat gun to better replicate the heating rate of conventional synthesis while simultaneously applying MWR to investigate EM field effects. This allows for a more direct comparison between MWR-assisted and conventional nanoparticle growth. Mixed heating conditions were implemented with an MWR power of 40 W and a 5 sec on/off pulse period and heat gun temperatures of 150°C. In both MWR-only and mixed heating experiments, MWR was introduced 1 minute after PDF acquisition began. Conventional heating was introduced immediately upon starting PDF data acquisition. A reaction time of 35 minutes was used for all conditions.

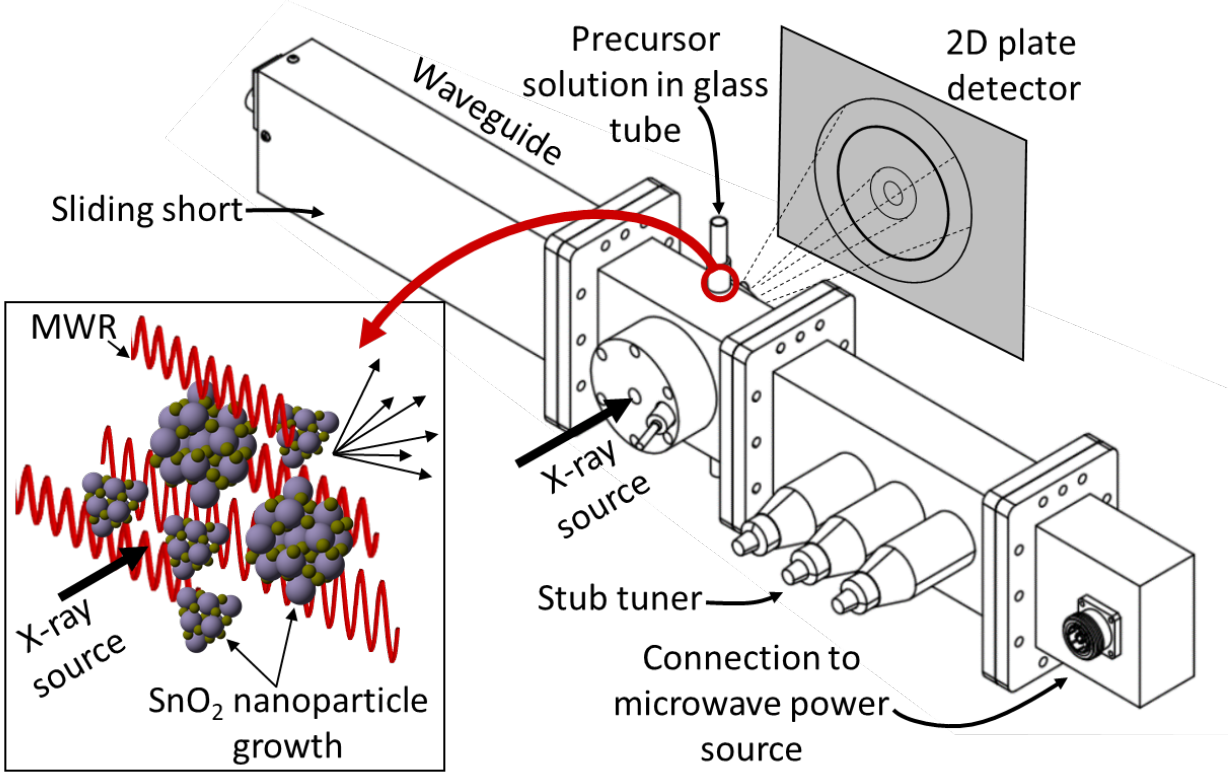

Figure 10: Custom-built waveguide enabling *in-situ* x-ray scattering experiments during MWR-assisted synthesis. Precursor solutions are held in a borosilicate glass tube aligned with the x-ray inlet and outlet ports. The inset displays the process of x-ray scattering during MWR-assisted nanoparticle synthesis occurring inside the reaction tube. A sliding short and stub tuner enable adjustable waveguide length and optimal MWR absorption by the sample, respectively. The waveguide is supplied MWR at a frequency of 2.45 GHz via a coaxial cable connection to a solid state microwave power source. This reactor was designed in collaboration with Gerling Applied Engineering.

The formation of crystalline rutile SnO_2 nanoparticles from the aqueous precursor was successfully monitored during conventional hydrothermal synthesis (Fig. 11a). The first step in our PDF analysis is to effectively characterize the structure of the aqueous precursor solution. The precursor structure was approximated using a *mer*-$[SnCl_3(H_2O)_3]^+$ complex, which prior *in-situ* PDF studies during high-pressure hydrothermal synthesis have identified as a suitable descriptor of the aqueous solution used.[27] Refinements using the *mer*-$[SnCl_3(H_2O)_3]^+$ structure utilized a scale factor, Sn-O and Sn-Cl bond distances ($d_{Sn\text{-}O}$, $d_{Sn\text{-}Cl}$), and anisotropic atomic displacement parameters (ADPs). ADPs were restrained based on whether their vibrations are longitudinal (U_l) or transverse (U_t) to the bond direction. H atoms were omitted, as they have a negligible effect on the measured PDF due to their weak x-ray interaction. This approach suitably models the nearest neighbor Sn-Cl and Sn-O peaks but does not account for many structural features observed past 4 Å (Fig. 11b).

The inability of our model to fit these higher-*r* features can be attributed to the lack of complexity in our starting model. Previous Nuclear Magnetic Resonance (NMR) spectroscopy studies have demonstrated that 1 M aqueous tin chloride solutions contain a mixture of $[SnCl_{6-n}(H_2O)_n]^{n-2}$ and $[Sn(H_2O)_{6-y}(OH)_y]^{(4-y)+}$ complexes.[28] While $[SnCl_3(H_2O)_3]^+$ is present in the highest percentage, it constitutes only approximately 40% of the complexes present and thus is unlikely to fully represent the experimental data. Additionally, we observe broad peaks in the PDF at *r* values larger than the size of any single precursor complex. These peaks may be caused by interparticle correlations,[29, 30] and are not modeled in the current framework. Additional low-intensity oscillations in the measured PDF may also be due to termination ripples caused by the finite *Q*-range of the experimental PDF measurements.[31] Despite these shortcomings, the current model well represents the Sn-O and Sn-Cl bond distances, which are the most critical for observing the change in the

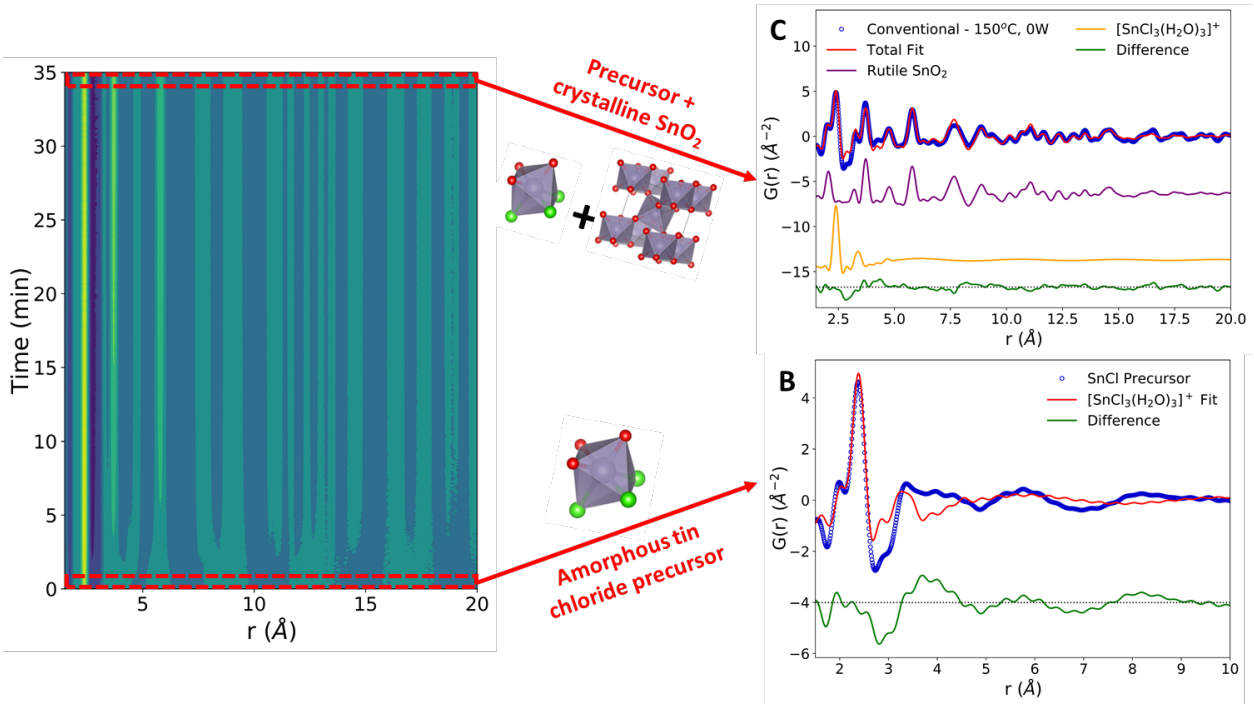

Figure 11: Conventional hydrothermal SnO_2 nanoparticle synthesis. (a) Contour plot demonstrating the growth of crystalline PDF peaks over time. (b) Experimental PDF data from the tin chloride precursor solution (blue) with the refinement to the $[SnCl_3(H_2O)_3]^+$ complex (red). The difference between the experimental data and the fit is shown offset below in green. (c) PDF data of the final synthesis product (blue) refined to a two-phase model (red). The total two-phase fit is a mixture of the crystalline rutile phase (purple) and the $[SnCl_3(H_2O)_3]^+$ complex (orange). The difference from the total fit is shown offset below in green.

precursor during synthesis. Therefore, fitting to only the $[SnCl_3(H_2O)_3]^+$ complex provides an adequate descriptor of the precursor structure and allows us to monitor structural changes during synthesis. The precursor structure observed prior to conventional synthesis is found to be consistent across all datasets collected.

The conventional synthesis experiment results in the formation of a crystalline rutile phase (Fig. 11c). The rutile phase was modeled by refining to lattice parameters (*a, c*), a scale factor, a low-*r* correlation parameter (δ_1),[32] spherical particle size,[33] and isotropic atomic displacement parameters (U_{iso}) for Sn and O atoms. All refinements to the final synthesis product include both the crystalline rutile phase and the amorphous $[SnCl_3(H_2O)_3]^+$ complex. Observation of peak intensities before and after SnO_2 crystallization reveals that the rutile Sn-Sn and Sn-O peaks form without a significant decrease in the Sn-Cl peak intensity (Fig. 12). Post-synthesis, the Sn-Cl peak has been labelled as Sn-C/O due to the potential for overlap in Sn-Cl, Sn-O, and O-O interatomic distances in this *r*-range. The slight shift in the Sn-Cl/O peak observed can be attributed to this peak overlap or changes in the Sn-Cl bond distance.

The high intensity of the final Sn-Cl peak indicates that the rutile SnO_2 formation mechanism during conventional heating is based in reorganization of Sn-O octahedral units present in the $[Sn(H_2O)_{6-y}(OH)_y]^{(4-y)+}$ complexes, not in the breaking of Sn-Cl bonds present in the $[SnCl_{6-n}(H_2O)_n]^{n-2}$ complexes. Therefore, the $[SnCl_{6-n}(H_2O)_n]^{n-2}$ complexes are not active during conventional hydrothermal SnO_2 phase formation. This finding aligns with prior results from conventional hydrothermal synthesis experiments utilizing an identical chemical precursor at concentrations of 2 and 4 M,[27] validating the *in-situ* data collection performed in our custom reactor. However, the previous work pressurized the reaction to 250 bar, while our synthesis system applies no external pressure and has an upper pressure limit of 15 bar set by the borosilicate reaction tubes. This demonstrates that the formation mechanism of rutile SnO_2 from aqueous tin chloride solutions during conventional hydrothermal synthesis remains similar even under relatively mild conditions. This validation of the rutile SnO_2 formation mechanism under conventional heating conditions allows for a direct comparison with the synthetic pathway during MWR-assisted synthesis.

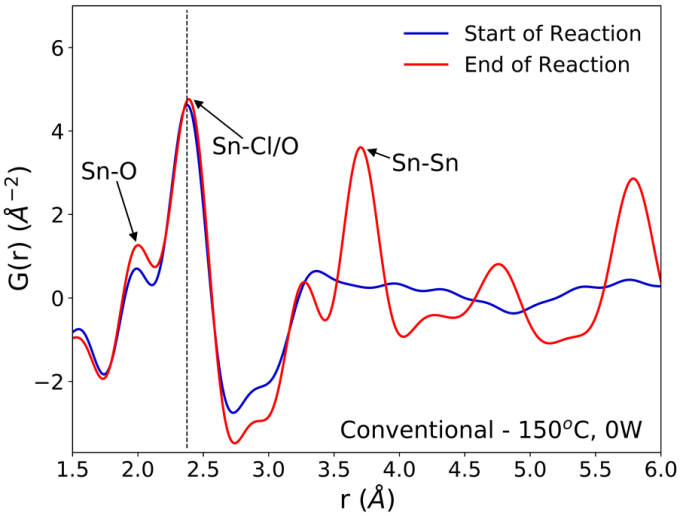

Figure 12: A comparison of the beginning and end of the reaction for conventional SnO_2 nanoparticle synthesis. The final product displays an increase in Sn-Sn and Sn-O peaks corresponding to rutile SnO_2 without any decrease in the Sn-Cl/O peak intensity. A slight increase in the Sn-Cl/O peak position and intensity is observed. This could be due to changes in the Sn-Cl bond length and overlap of Sn-O and O-O peaks at these interatomic distances.

We observed that SnO_2 nanoparticle synthesis was clearly influenced by the presence of MWR, resulting in enhanced growth relative to conventional hydrothermal synthesis. Two MWR-assisted synthesis conditions were used, with both resulting in improved nanoparticle growth: (1) MWR-

only and (2) mixed MWR-conventional. The mixed heating condition was used to provide a heating rate similar to conventional experiments, allowing for a more direct comparison between the heating profiles. The MWR-only condition is unable to replicate this heating profile due to the pulsed nature of MWR deposition but demonstrates improved SnO_2 growth despite the slower heating rate.

In all experiments with MWR exposure, the final crystalline phase observed remains rutile. No significant differences in the rutile lattice parameters are observed between conventional and MWR-assisted synthesis. However, significant differences in the final Bragg peak intensity and broadening exist in the raw total scattering data (Fig. 13a). MWR-assisted experiments contain sharper, higher intensity Bragg peaks, indicating larger SnO_2 nanoparticle sizes. This is confirmed

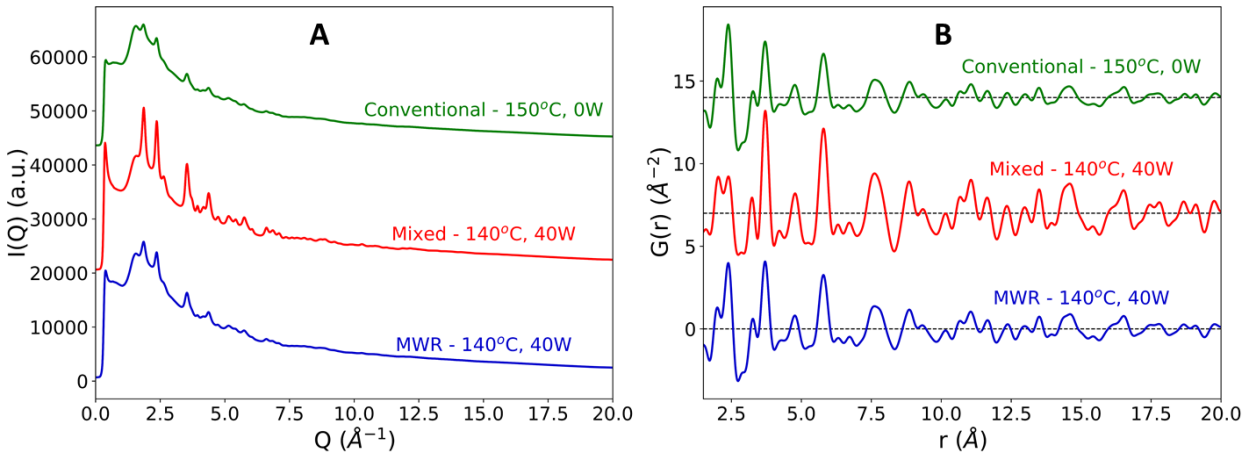

Figure 13: (a) Raw total scattering data, *I(Q)*, for the conventional (green), mixed MWR-conventional (red) and MWR-only (blue) synthesis conditions. Sharper peaks are present in the final product for MWR-grown samples. (b) PDF data, *G(r)*, for the same datasets as in (a). The increase in Bragg intensity shown in (a) is found to be due to an increase in particle size, as seen by the increase in intensity of peaks at higher *r* values for samples grown by MWR-assisted synthesis.

via PDF analysis, where the final product for the MWR-assisted samples display higher intensity rutile peaks out to larger-*r* values, which is indicative of larger nanoparticle sizes (Fig. 13b).

PDF refinements over the entire reaction time confirm the MWR-enhanced nanoparticle synthesis, with faster growth and larger particles observed under MWR exposure (Fig. 14). The final nanoparticle size for MWR-only and mixed heating conditions were 25.1 and 32.4 Å, respectively. Conventional heating results in a particle size of 23.5 Å. The rutile phase was included in refinements at the time which rutile peaks became clearly visible, leading to a predicted particle size of 0 Å before this time. Particle size information is available at earlier times under conditions with conventional heating due to the nature of the experimental setup. Conventional heat is introduced to the system immediately upon starting PDF data acquisition, while MWR is applied approximately 1 minute after data acquisition has begun. This leads to a longer delay time at room temperature in the MWR-only condition, and thus a slightly delayed start to phase formation. Due to the slower heating rate associated with the MWR-only condition, more time is spent at lower

synthesis temperatures. This explains the smaller particle size of the MWR-only condition relative to the mixed heating condition, which reaches its steady-state temperature quickly and thus applies MWR while maintaining a higher synthesis temperature. However, both MWR-assisted conditions outperform the conventional synthesis experiment.

Enhanced SnO_2 nanoparticle growth occurs despite MWR-assisted synthesis occurring at similar temperatures than the conventional heating experiment. This behavior contrasts conventional nanoparticle growth, where higher synthesis temperatures regularly correspond to larger particles.[27, 34-36]

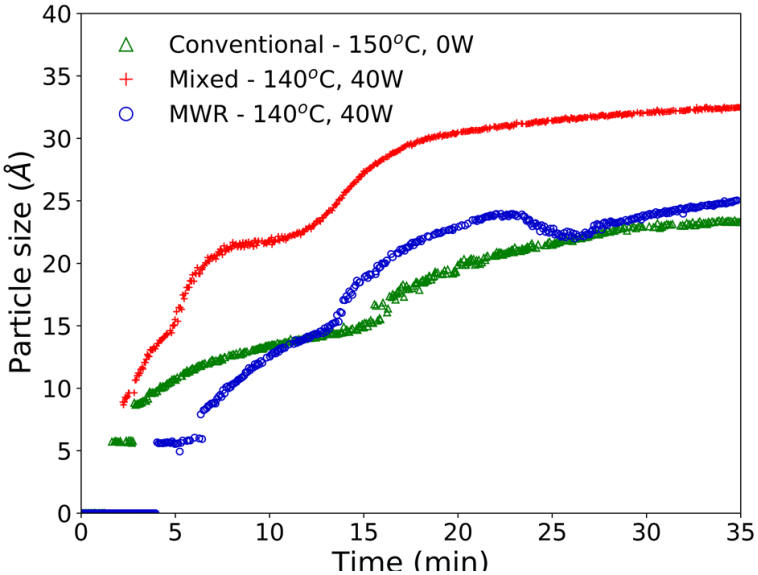

Figure 14: Spherical particle diameter for SnO_2 nanoparticles synthesized conventionally without MWR exposure (green), with mixed MWR-conventional heating (red), and with only MWR exposure (blue). The presence of MWR promotes larger nanoparticles and more rapid growth relative to conventional synthesis at similar temperatures, indicating an effect of MWR on growth. The delay in nanoparticle growth for the MWR-only samples is due to a delay in the beginning of MWR exposure during synthesis.

The enhanced nanoparticle growth observed during MWR occurs at similar temperatures to conventional synthesis, indicating that the presence of MWR is driving SnO_2 synthesis. This invites discussion into the mechanisms underlying rutile SnO_2 phase formation under MWR exposure. To study the origin of the observed change in kinetics, the ADPs and local atomic structure were studied via PDF analysis. The ADP, U_{iso}, is obtained from PDF refinements and represents the average displacement of atoms from their expected lattice position.[31] U_{iso} encompasses both thermal vibrations and static displacements. Thus, U_{iso} will be higher in systems at higher temperatures or with more structural disorder. Sn U_{iso} values converge to similar values regardless of synthesis conditions (Fig. 15a). The high values at short synthesis times and subsequent decay can be attributed to the crystallization process. Rutile will not be fully crystallized or particle sizes will be extremely small at early reaction times, leading to a distorted structure and broader PDF peaks that are accommodated in the refinement process by high U_{iso}

values. As nanoparticles grow and rutile crystallizes, the Sn displacement parameters converge to reasonable values.

The O U_{iso} values, however, are significantly impacted by MWR. The presence of MWR leads to two pronounced peaks in the displacement parameter, while O U_{iso} displays only one broad peak during conventional heating (Fig. 15b). The timing of peaks in O U_{iso} during MWR-assisted synthesis also correspond well to the initial formation of the first two rutile Sn-Sn interatomic distances (Fig. 16a-b). The peak in oxygen displacement during conventional synthesis is lower in magnitude than that which occurs under MWR exposure and occurs slowly over more than half the total synthesis time (Fig. 16c). The larger magnitude of the O U_{iso} peak during EM field exposure occurs despite the similar temperatures across all synthesis experiments, indicating that the additional contribution to U_{iso} is due to static disorder on the oxygen sublattice. This suggests that MWR exposure induces significant reordering of the oxygen sublattice which promotes the enhanced SnO_2 nanoparticle growth observed.

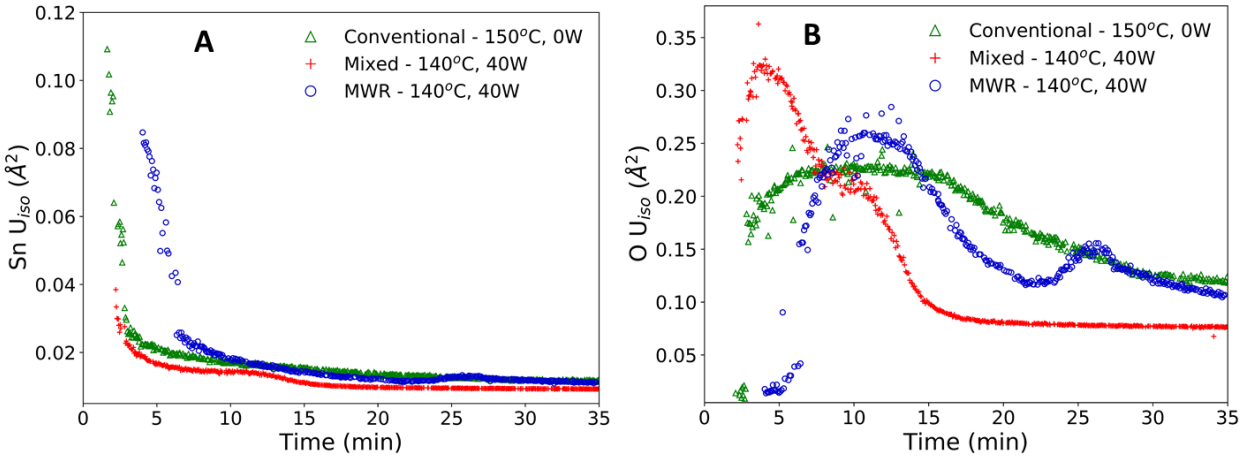

Figure 15: (a) Sn atomic displacement parameters *(U_{iso})* for conventional (green), mixed (red), and MWR-only (blue) synthesis conditions. (b) O U_{iso} values for the same reaction conditions shown in (a). The presence of multiple peaks in O U_{iso} during MWR-assisted reactions indicates changes on the oxygen sublattice not present during conventional hydrothermal conditions.

This figure depicts our strongest evidence that electromagnetic fields (including low energy microwave radiation) can affect atomic positions. We believe this result represents the most important finding of our YIP project.

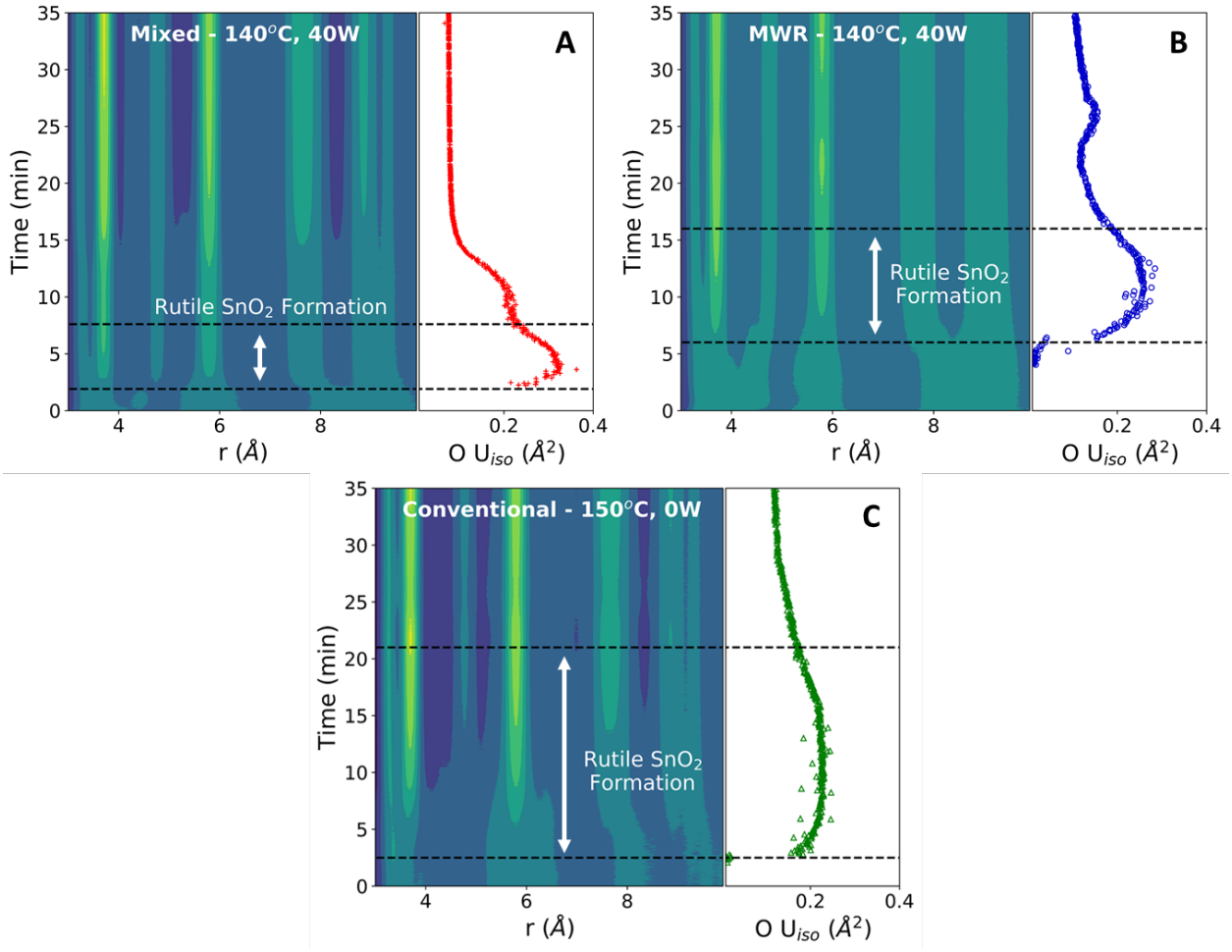

Figure 16: Contour plots of mixed (a), MWR-only (b), and conventional (c) synthesis conditions compared with O U_{iso} during the same time period. Sharper peaks in the displacement parameter are observed during MWR-assisted synthesis and correspond to an increase in intensity of the first two Sn-Sn peaks. Conventional synthesis results in a broad, lower-intensity peak in U_{iso} which exists throughout over half the total reaction time.

To further investigate the changes in local structure during phase formation, we utilize a difference PDF method to highlight subtle structural changes.[37] The difference PDF, *ΔG(r)*, is given by:

$$\Delta G(r) = G(r) - G(r)_{t=0}$$

Where $G(r)_{t=0}$ is the PDF data at the start of the reaction, and *G(r)* is any PDF after t=0. This method monitors only changes from the initial precursor structure. Thus, positive peaks indicate more interatomic distances forming at that *r* value relative to the initial tin chloride precursor, and negative peaks indicate a loss of interatomic distances (Fig. 17).

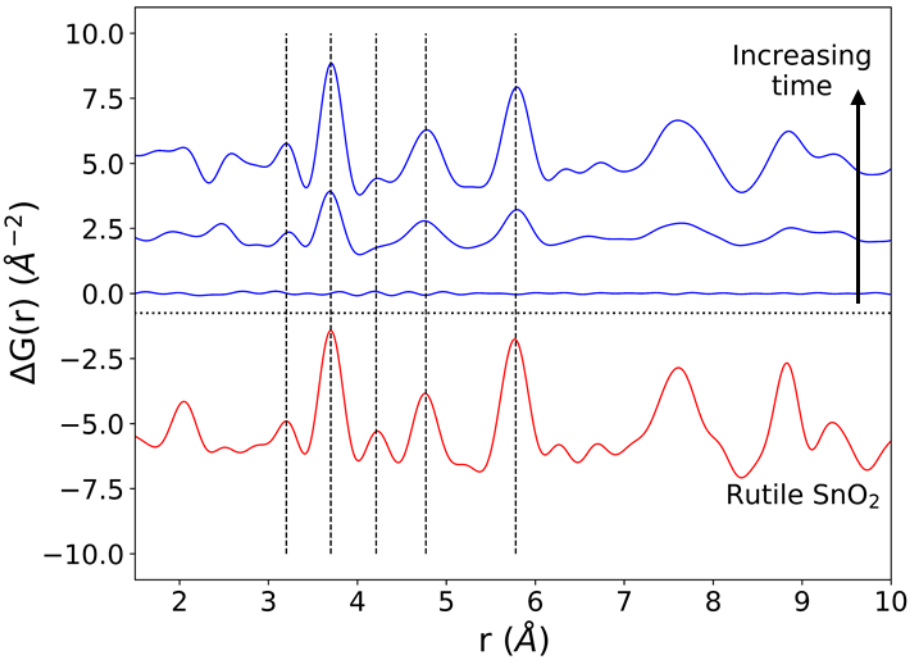

Figure 17: Demonstration of the *ΔG(r)* method, used to highlight changes from the initial precursor structure. At early reaction times, no structural changes have occurred and *ΔG(r)* (blue) remains flat. Over time, peaks corresponding to rutile increase in intensity. This indicates the formation of interatomic distances that match with rutile during synthesis. Select rutile interatomic distances are denoted by vertical dashed lines, and a calculated PDF of the rutile structure is shown offset below in red.

ΔG(r) data is analyzed over the entire reaction time to observe changes in the local atomic structure during synthesis (Fig. 18). For both the MWR-only (blue) and mixed heating (red) conditions, clear shifts in the nearest neighbor Sn-O and Sn-Sn peak positions are observed. The Sn-O peak in MWR-assisted conditions moves to a slightly larger *r*-value, while the Sn-Sn peak exists at a smaller interatomic distance than the conventionally synthesized SnO_2. Additionally, the Sn-Cl/O peak in ΔG(r) becomes negative during MWR-assisted reactions. The Sn-Cl bond distance provides the most significant contribution to this peak, indicating a loss of Sn-Cl bonds in the precursor complex. The decrease in Sn-Cl intensity suggests a mechanistic change under EM field exposure in which the Sn-Cl bond in $[SnCl_{6-n}(H_2O)_n]^{n-2}$ complexes are involved in phase formation. This differs from the proposed mechanism for conventional hydrothermal synthesis found both here and previously, which indicates that SnO_2 crystallizes via reorientation of pre-existing Sn-O octahedra.[27] Additional low-intensity peaks also appear in the region near the Sn-Cl peak (2.5-2.9 Å) in MWR-grown samples that are not present during conventional synthesis (dashed box in Fig. 18). Due to the potential overlap of Sn-Cl, Sn-O, and O-O peaks in this *r*-range, it is difficult to assign specific interatomic distances to these peaks. However, their presence indicates the formation of interatomic correlations not present in conventionally synthesized samples.

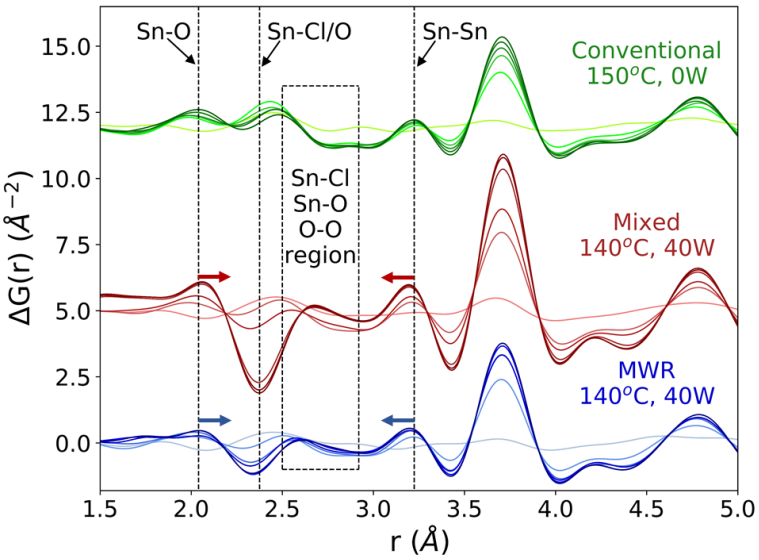

Figure 18: *ΔG(r)* throughout rutile phase formation for conventional (green), mixed (red), and MWR-only (blue) synthesis conditions. Lighter colors correspond to earlier reaction times, and become darker as the synthesis progresses. Dashed lines indicate the nearest neighbor Sn-O, Sn-Cl/O, and Sn-Sn distances. Shifts in the Sn-O and Sn-Sn peaks for MWR-assisted samples are denoted by colored arrows. The 2.5 to 2.9 Å region (dashed box) displays low-intensity peaks during MWR-assisted conditions which are not present during conventional synthesis.

The changes in Sn-O, Sn-Sn, and Sn-Cl nearest neighbor distances and high rutile O U_{iso} values during MWR-assisted synthesis indicate a change in the phase formation mechanism relative to conventional hydrothermal synthesis. One potential source of the observed differences is alterations in the local Sn-O coordination environment during rutile phase formation. Generally, tin oxide materials contain structural units with either octahedral or tetrahedral Sn-O coordination. The rutile structure is composed of a mixture of corner and edge-sharing octahedra.[38] However, intermediate SnO and Sn_3O_4 phases have been identified as having tetrahedrally coordinated Sn-O units, which alters the Sn-O and Sn-Sn nearest neighbor distances.[39-41] Changes in coordination environment during rutile growth would also require restructuring of oxygen atoms, and could explain the high O U_{iso} values observed prior to rutile formation.

The Sn_3O_4 intermediate can also be described by a large amount of ordered oxygen vacancies in the rutile lattice.[42] While we do not observe any intermediate phase in our experiments, point defects would impact local Sn-O coordination and alter nearest neighbor distances even without formation of an SnO or Sn_3O_4 phase. The role of point defects in distorting local atomic structure has been demonstrated in many other oxide materials.[18, 43, 44] Additionally, oxygen point defects represent a form of static disorder which would lead to high O U_{iso} values during rutile phase formation. The decrease in the Sn-Cl peak may also be correlated with oxygen atoms leaving the

rutile lattice. A decrease in the number of Sn-Cl bonds indicates a transition to higher values of *n* in the $[SnCl_{6-n}(H_2O)_n]^{n-2}$ complexes present in the precursor. Higher *n* values result in the transition of $[SnCl_3(H_2O)_3]^+$ into a $[SnCl_2(H_2O)_4]^{2+}$ complex. This transition involves the loss of one Cl atom and the addition of one O atom. While this explanation is certainly over-simplified relative to the true solution chemistry, it provides an example of how oxygen vacancies in the rutile structure could correlate to a decrease in Sn-Cl bonds in the precursor solution.

SnO_2 is an *n*-type semiconductor and is easily reduced, increasing the likelihood that oxygen vacancies could be generated during EM field-assisted synthesis.[45-47] Oxygen vacancies in many other oxide systems have also been found to act as nucleation sites promoting phase formation.[16, 48-51] Therefore, oxygen vacancy formation provides a plausible explanation for the changes in interatomic distances, high U_{iso} values, decrease in Sn-Cl peak intensity, and enhanced rutile phase formation observed. This aligns well with prior studies on EM field-assisted methods, which have obtained evidence for oxygen defect-mediated reactions but were not able to characterize the local atomic structure.[22, 52-55] Nanoparticle size effects may also influence the local structure and contribute to changes in the interatomic distances in both MWR-assisted and conventionally synthesized SnO_2.[56-59] The relationship between the size and structural disorder in MWR-assisted nanoparticles warrants further investigation.

The decrease in the Sn-Cl peak intensity and high oxygen displacements observed during EM field exposure invites discussion regarding how an applied EM field may influence specific atomic species relative to conventional heating. While the full impact of EM fields during synthesis remains an open question, the polarizability of specific ions and the atomic structure may contribute. Prior work has demonstrated that Cl and O species are more polarizable than cations such as Sn, which would lead to a stronger interaction with an applied EM field.[60, 61] Highly electronegative atoms such as O and Cl will also attract electrons relative to Sn, resulting in polarization of the Sn-O or Sn-Cl bond.

In a perfect rutile crystal, this polarization will cancel out due to the symmetry of the crystal structure. However, distorted or defective structures which occur during phase formation will impact this symmetry, potentially resulting in more polarizable atomic configurations. Indeed, previous studies have demonstrated that defects in metal oxide crystals can result in increased polarizability and that polarization effects can lower vacancy formation energy.[62] This suggests that the polarizability of both the individual ionic species and atomic structure may be important factors underlying EM field-assisted synthesis. Further investigations on the interplay between polarization, charge distribution, applied EM fields, and structural distortions are needed to fully understand the observed effects. However, the results presented here support the notion that local polarizability may be an important factor in understanding structural changes during EM field-assisted synthesis.

5.3 Decoupling thermal and non-thermal effects during EM field processing using a split ring resonator (SRR) system

Results:

SRRs contain a gap region in which large electric fields can be localized and intensified (exceeding 10^7 V/m in air) without significant thermal loading. Varying the ring size and/or material tunes the intensity, frequency, and polarization of this EM field. As described above, EM fields tend to heat the sample that is under investigation, making it difficult to distinguish the contributions of thermal effects (e.g., volumetric heating) from matter-field coupling, non-thermal effects.

To demonstrate that the resonators were generating fields of this intensity, a proof-of-concept experiment using tungsten oxide (WO_3) powder was designed. WO_3 powder is electrochromic; when an electric field is applied to this material, it changes color. If it can be shown that when an electric field is passed through the SRR, WO_3 powder within the gap changes color, this is evidence that powder samples can interact properly with the field generated in this gap. By using a combination of a Canon DSLR T7i camera and a Canon EF 100mm f/2.8 Macro USM Lens, imaging of the SRR gap with < 5 μm resolution is made possible (see Fig. 19b below). A very small amount of WO_3 powder is placed in the gap (ball-milled to reduce the particle size) by first suspending the powder in acetone, then using a micropipette to place 10 μL of this solution in the gap. Images of the WO_3 powder were captured before, during and after application of the electric field, which shows the color transition from blue to green (see Fig. 19c-e, where powder is enclosed inside the red box). Note that the powder outside this gap did not change color (see left side of Fig. 19e). This color change confirms that there is a high intensity field inside the gap that is indeed interacting with powder samples placed within this region. With this preliminary result in mind, testing of other powders, liquids and thin film samples in the gap can begin.

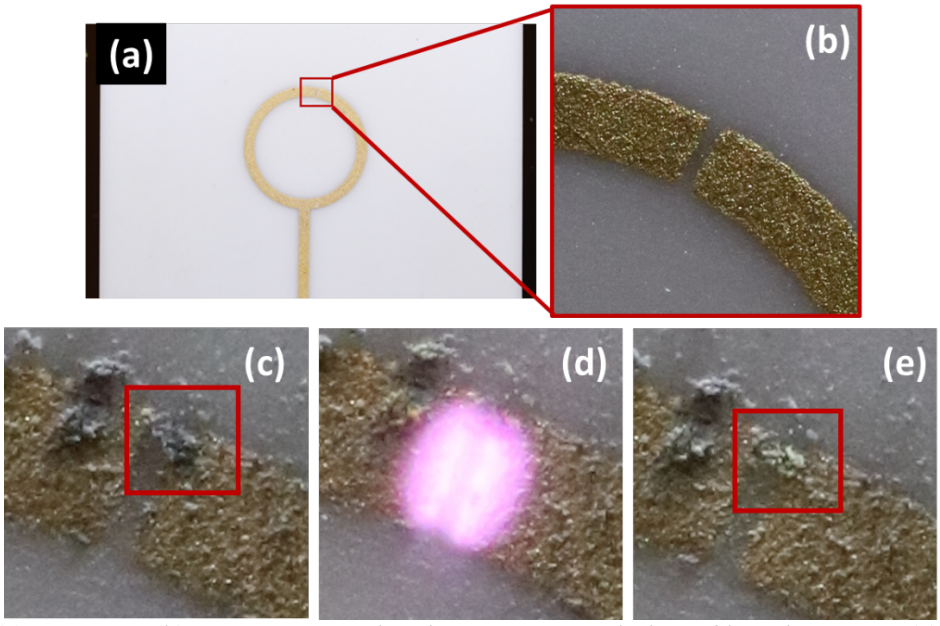

Figure 19: (a) SRR 6-7. (b) SRR 6-7 gap, showing < 5 μm resolution of imaging setup. (c) SRR 6-7 gap before field application, blue WO_3 powder highlighted. (d) Gap during field application, showing plasma striking. (e) After field application, with green WO_3 powder highlighted.

*We collaborate extensively with Dr. Michael Lanagan at Pennsylvania State University.

Next steps for 2020:

By identifying mechanisms by which EM fields can intensify within the multiscale structure of a material, the proposed tasks can facilitate quantifying the *far-from-equilibrium* effects of such fields. We have shown in the case of WO_3 powder that our current experimental setup can successfully apply these fields to our sample of interest. This proof of concept demonstrates that non-thermal effects of EM fields can be observed by inserting different materials into the gap. Rutile powder (a thermodynamically stable atomic structure of TiO_2) will be inserted into the gap and the field will be applied. Based on previous work described in Task 1, a phase transformation to anatase is expected (a metastable structure of TiO_2). Inserting the powder into the gap, applying the electric field through the SRR and irradiating the rutile powder allows for the *ex-situ* observation of the phase change to anatase through X-Ray Diffraction (XRD) and/or Pair Distribution Function (PDF). Because we can decouple the thermal and non-thermal effects acting on this powder, these experiments can provide insight on the underlying fundamental mechanisms in field, temperature, and frequency space. This work thus lays the theoretical foundations for deploying EM fields as a new processing tool to access high temperature ceramic phases with minimal thermal input, allowing access to phase space, microstructures, and properties inaccessible via conventional synthesis routes.

We are also interested in experimenting with the potential to manufacture micro plasma treatment devices using the SRRs. This is supported by the previous results that showed how powders placed in the gap were influenced by the EM field that the SRR generates. The ability to change the plasma characteristics, this can be a tunable technology that can be implemented when you would like to plasma treat a material using very specific parameters. For example, the atmosphere can be changed to house different gases (N_2, SF_6, etc.) which will affect plasma properties such as ignition power, electron temperature, etc. Studying how non-ceramic powders influence the plasma properties will also be useful in developing these systems, beginning with noble metals such as Ag and Au. This would tell us whether this SRR micro plasma treatment system can treat a wider variety of materials than we have confirmed thus far. After the EM field effects on powders are observed, the next step will be thin film samples/liquid samples. By gathering data on samples over a range of material systems (ceramics, metals) and preparations (powder, thin film, liquid) we can begin to explain how and why EM fields trigger transformations at the electronic, ionic or molecular length scales as a function of field parameters (e.g. intensity, frequency, polarization).

5.4 Dielectric characterization and polarization mechanism analysis of Al_2O_3 single crystals at W-band frequencies (75-110 GHz)

Results:

The dielectric anisotropy of Al_2O_3 is studied here by characterizing W-band (75-110 GHz) complex permittivity of four different orientations of sapphire (Al_2O_3 single crystals). This was done using free-space, focused beam methods. Dielectric polarizability (α_D) of these orientations is then calculated and these values are related to their complex permittivity. Based on this relationship, a framework is developed for rapid and straightforward estimation of dielectric anisotropy using a known crystal structure and a dielectric permittivity measurement performed on one orientation of the material. This framework can be applied to other materials with dielectric anisotropy (e.g., SnO_2, $LiGaO_2$) to predict permittivity for different orientations, enabling rapid

design of high-frequency systems (e.g., radomes, wavelength-selective windows). These permittivity measurements were also used to determine the dominant polarization mechanisms leading to dielectric anisotropy of Al_2O_3 in the W-band; electronic and ionic polarization orthogonal to the direction of the focused beam (i.e., the direction of the electric field).

To study the dielectric anisotropy and polarization mechanisms dominant in Al_2O_3 at W-band frequencies, we performed measurements of complex permittivity for four orientations of sapphire. We subsequently compared these values with the calculated dielectric polarizability for these orientations using a two-dimensional procedure adapted from three-dimensional dielectric polarizability theory.[63] The following sections describe the trends we observed when comparing the polarizability and permittivity of different orientations in Al_2O_3.

Prior studies have characterized the relationship between bulk permittivity and polarizability but have never applied this approach to study the anisotropy of permittivity. Figure 20 shows the different orientations of Al_2O_3 that were characterized in this work. We also used the results from these planes to study the dominant polarization mechanisms in Al_2O_3 at W-band frequencies.

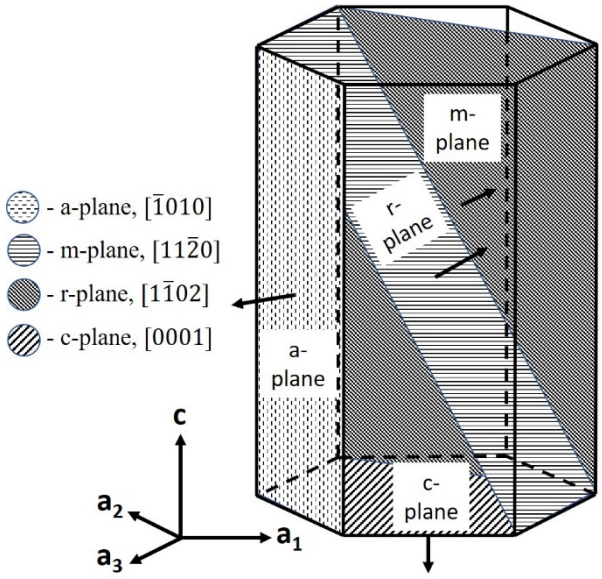

Figure 20: Al_2O_3 unit cell displaying the different orientations of sapphire (Al_2O_3) used here, c- a- r- and m-plane, their Miller indices and the directions normal to these orientations (black arrows).

The polarizability was calculated for different orientations of sapphire using the Al_2O_3 unit cell and previously tabulated ion polarizabilities.[64] This was done to study the relationship between polarizability (α_D) and permittivity (ε') in anisotropic materials, allowing for estimation of ε' values for different orientations. This relationship is plotted in Figure 21, where a positive correlation between α_D and ε' is observed (as α_D increases ε' increases).

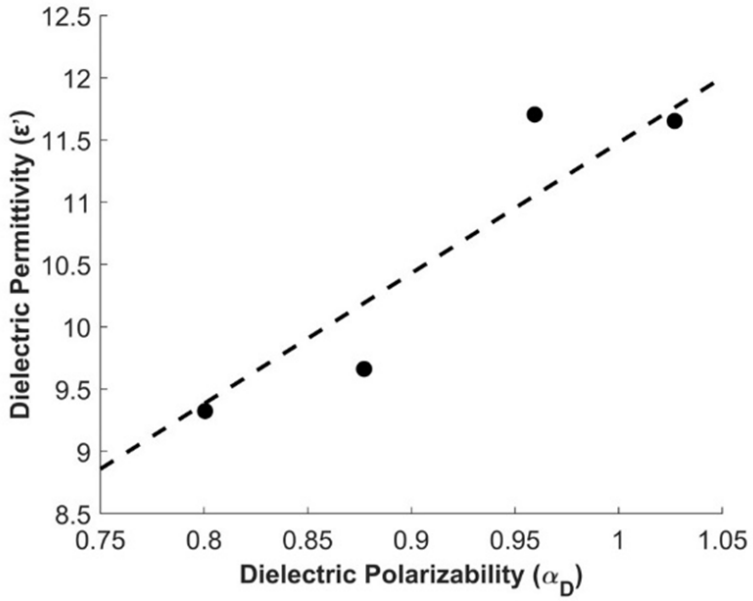

Figure 21: Dielectric permittivity as a function of dielectric polarizability, $\varepsilon'(\alpha_D)$, for four orientations of sapphire. These values of α_D are considering planes parallel to incident wave (i.e., planes orthogonal to electric field direction) and therefore orthogonal to the electric field. A positive trend is seen, where an increase in α_D leads to a linear increase in ε'. It is observed by extrapolation of the trendline in that $\varepsilon'(\alpha_D = 0) = 1$, which is the case for vacuum. This serves as a further verification that our framework is predicting accurate values of permittivity.

This relationship can be explained by reviewing the major polarization mechanisms in low conductivity materials under moderate electric fields (i.e., at fields much lower than the inner atomic or molecular fields). Potential mechanisms include electronic, ionic, orientational (i.e., dipole rotation), hopping, and space charge polarization.[65] Orientational polarization is not present due to insufficient degrees of freedom in the Al_2O_3 coordination 28olyhedral. Hopping and space charge polarization can be ruled out as well, as they are relaxation processes and the high frequency of the field does not give adequate time for relaxation. If these mechanisms were active, we would see a change in ε' with frequency because higher frequencies would increase the rate of these processes, which is not observed. The remaining mechanisms are electronic and ionic polarization.

A verification of the dominant polarization mechanisms was done using refractive index (n) data. ε' can be calculated from n using $\varepsilon' = n^2$, assuming we do not have any relaxation mechanisms active (i.e., electronic and ionic mechanisms only)[65]. Literature data exists on n of bulk Al_2O_3 at W-band[66, 67], so we perform this analysis using our polycrystalline Al_2O_3 data. The n of polycrystalline Al_2O_3 is reported as 3.047 across the entire W-band[66], which yields $\varepsilon' = 9.284$ (within 5% of our measured ε'). This verifies that the dominant polarization mechanisms in Al_2O_3 at W-band frequencies are electronic and ionic polarization.

Given that electronic and ionic polarization are the dominant mechanisms, it becomes necessary to investigate how much each mechanism contributes to the total polarizability. A quantitative analysis of these contributions can be accomplished by considering the refractive index (n) of Al_2O_3 at optical frequencies. At optical frequencies (where there is no ionic polarization), n will only contain contributions from electronic polarization. The ionic contribution to ε' at W-band frequencies can be calculated from the difference between our measured ε' at W-band frequencies and the literature value of n^2 at optical frequencies. The n is 1.7708 at the optical frequency of 549 THz[68], allowing us to conclude that in Al_2O_3 at W-band frequencies, the polarization is approximately 32% electronic and 68% ionic. Future experiments will allow us to find n of different orientations at optical frequencies, then calculate whether the relative contributions of the electronic and ionic mechanisms change with orientation.

Our results suggest that the property influencing the ε' in Al_2O_3 is the polarizability of the planes parallel to the incident wave (Figure 21). This is due to polarization acting primarily in the direction parallel to the electric field, orthogonal to the incident wave. Once an electric field is introduced, electronic polarization is activated; the centers of the electron clouds in the Al^{3+} and O^{2-} ions are shifted so that they do not coincide with the positive nuclei, leading to polarization. This occurs in the direction of the electric field, where the nucleus is dragged in the negative direction of the electric field relative to the center of the electron cloud. Ionic polarization is then activated; because the O^{2-} electron clouds (shifted in the positive direction) are now closer to the nuclei of the Al^{3+} ions (shifted in the negative direction), these ions are more attracted to each other, leading to polarization. This polarization occurs along the bond directions[65], which are close to but not exactly aligned with the electric field, which explains the slight deviations from the trendline in Figure 21.

To investigate the generalizability of our approach used to characterize the dielectric anisotropy of Al_2O_3, we applied our framework to other material systems using dielectric constant data from the literature. Dielectric constant data of SnO_2[69] and $LiGaO_2$ [70] were chosen for comparison because they demonstrate strong dielectric anisotropy. W-band data was not available, so measurements made in different frequency regimes were used. The same trend seen for Al_2O_3 was observed, where α_D and ε' are linearly proportional. Figure 16 plots the dielectric permittivity data for different orientations as a function of the calculated dielectric polarizability. When the trendlines for all materials are extrapolated to $\alpha_D = 0$, ε' converges to 1, which is ε' of vacuum. α_D of vacuum is zero because there is nothing polarizable in the medium. The good fit of the trendlines (e.g., for SnO_2, $R^2 = 0.998$) and their convergence at $\alpha_D = 0$ are indicators that this framework is applicable to other materials as well. Our results suggest that this framework can be used on materials that have slight deviations from the 'well-behaved' criteria presented by Shannon[71], but how far they can deviate is yet to be tested.

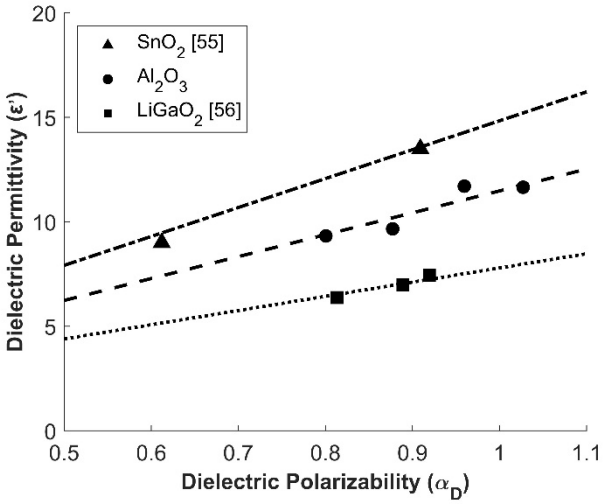

Figure 22: Dielectric permittivity vs dielectric polarizability for SnO_2, Al_2O_3 and $LiGaO_2$. All three materials see the same trend where an increase in α_D leads to a linear increase in ε'. It is also observed by extrapolation of the trendlines that $\varepsilon'(\alpha_D = 0) \approx 1.0$ for all three materials.

The anisotropy of permittivity in Al_2O_3 was investigated here to develop a framework that can relate the polarizability of orientations to their dielectric permittivity at W-band frequencies. The results were also used to study the dominant polarization mechanisms of Al_2O_3 at these frequencies. The complex permittivity of four orientations of sapphire was characterized using free-space, focused beam methods. Dielectric polarizability for these orientations were obtained by modifying the three-dimensional dielectric polarizability theory to obtain a two-dimensional framework. We find that as the polarizability of the planes parallel to the direction of the incident wave increases, the dielectric permittivity (ε') increases. These results present a rapid and straightforward method for estimating dielectric anisotropy without the need for large single crystals ($d > 3.05$ cm for the focused-beam setup used in this study), which are expensive or impossible to fabricate for some material systems[72]. This method also eliminates the need for several time-intensive permittivity measurements of different orientations or density functional theory (DFT) calculations[73].

The inputs to the framework are a well-characterized crystal structure and a dielectric permittivity measurement performed on one orientation of the material. By using α_D and ε' values of this orientation and $\varepsilon'(\alpha_D = 0) = 1$ to plot a trendline, one can extrapolate ε' for the other orientations. Future experiments will explore application of the framework to different frequency regimes and different material systems, as well as allow us to study what variables influence the slope of the α_D vs ε' trendline, eliminating the need for any dielectric permittivity measurements (rather than one). We also found that the dominant polarization mechanisms leading to dielectric anisotropy for Al_2O_3 in the W-band were electronic (~32%) and ionic (~68%) polarization. This work enables rapid design and evaluation of components in high-frequency systems, such as radomes and electromagnetic susceptors, especially in systems that use novel, poorly characterized materials.

A manuscript on this work has been published in 2019 and another will be submitted in 2020.

Next steps for 2020:

We present here an adaptable framework that calculates permittivity of different orientations in 'well-behaved' anisotropic materials. Future experiments will test the adaptability of this framework; different frequency regimes (e.g., S-band microwave frequencies, X-band, K-band, etc.) will be explored to see how the trend in α_D and ε' for sapphire will change. The framework may be complicated at these lower frequencies due to additional polarization mechanisms that are not active in the W-band. This framework may also be applied to polycrystalline materials with preferential growth directions (i.e., textured materials) in addition to single crystals. The orientation of these grains can be characterized using methods like electron backscatter diffraction mapping[74] or diffraction contrast tomography[75]. The net polarizability of the sample can then be computed by weighing the polarizability of different orientations by the proportion of this orientation in the sample using an additivity rule similar to a rule of mixing equation. Dielectric permittivity can then be calculated using this net polarizability. This approach may be complicated by space charge polarization[65] which can occur at the grain boundaries under lower frequency fields.

*We collaborate extensively with Dr. Brad Hoff's team at AFRL Directed Energy Directorate. M. S. Hilario and B. W. Hoff were supported by the U.S. DoD, AFOSR under award number FA9550-17RDCOR449. Maxwell R. Telmer was supported in part by the AFRL Directed Energy Summer Scholars Program in 2018-2020.

6. Objective 3: Apply resulting knowledge to synthesize far-from-equilibrium materials

The knowledge gained in Objective 2, namely that MWR-assisted synthesis is an oxygen defect mediated process and that defect formation is driven by high local field intensities, presents the opportunity to begin utilizing MWR in materials design. As described here, we began proof-of-concepts testing of such materials for applications in clean energy (e.g., batteries) during the last stage of the YIP project. We will pursue additional funding sources to continue this applied research.

6.1 Synthesis of sub-oxide Magneli phases

The ability of MWR to impact the oxygen sublattice makes it a natural choice to explore the synthesis of substoichiometric oxide materials, or suboxides. One such class of suboxides are Magneli phases. Magneli titania are Ti_nO_{2-n} phases that display high electrical conductivity and good electrochemical stability, making them highly desirable in a variety of applications.[76] Preliminary work in this area has led to conventional synthesis of Magneli suboxides in a reducing hydrogen environment without EM field exposure (Fig. 23).

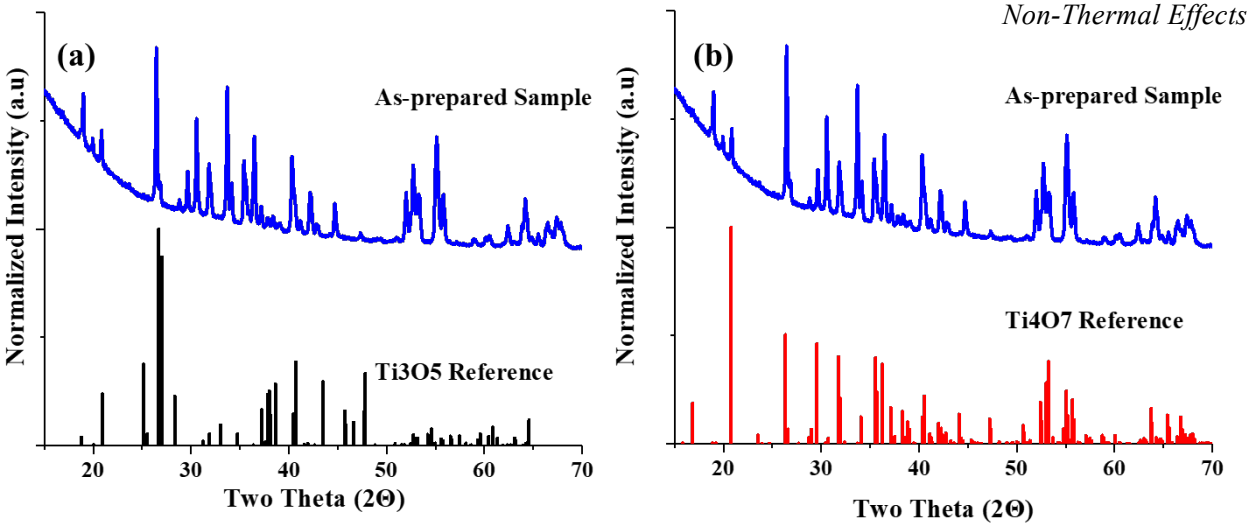

Figure 23: (a) Sub-oxide Magneli phase sample (blue) compared with a Ti_3O_5 reference (black). (b) The same as-synthesized sample (blue) compared with a Ti_4O_7 reference. The peak positions indicate a mixture of Magneli phases.

Moving forward, the goal is to combine this Magneli synthesis experience with our expertise in MWR-assisted synthesis to engineer suboxide titania phases with defect concentrations dependent on EM field conditions. Magneli phases are highly desirable due to their high electrical conductivity and good electrochemical stability, making them a promising material for Li-ion battery and fuel cell applications. The ability to rapidly synthesize Magenli phases at low temperature and with tunable defect concentrations based on EM field parameters would represent a significant advance.

6.2 MWR-based surface engineering of Li-ion battery electrodes

An additional application of MWR-grown oxide materials is in the surface engineering of Li-ion battery electrodes. The ability of MWR to impact phase formation and defects make it an intriguing option to explore for the design of surface coatings. We envision applying such TiO_2 and ZrO_2 coatings to the surface of battery electrodes like $LiCoO_2$ particles to explore the usefulness of MWR-assisted synthesis for Li-ion battery cathode surface engineering.

7. Conclusion

Over the course of this grant, we have successfully contributed insight into the atomistic mechanisms by which EM fields influence ceramic oxide materials. We have demonstrated that MWR-assisted synthesis reactions are an oxygen defect-mediated process, and that the concentration of these defects is dependent on the local electric field intensity. Additionally, we have shown how thermal and non-thermal effects can be decoupled using an SRR system, and how polarization mechanisms affect dielectric property anisotropy. This information was used as building blocks to develop novel *in-situ* instrumentation capable of monitoring electric fields and atomic structure in real-time during MWR-assisted synthesis. The culmination of these mechanistic insights has led to efforts to utilize EM fields to design materials with phase compositions or properties not readily accessible via conventional routes. Preliminary work has

demonstrated the usefulness of EM fields for the synthesis of sub-oxide phases, and as potential performance-enhancing surface coatings for Li-ion batteries.

References

1. K. I. Rybakov, E. A. Olevsky and V. E. Semenov, *Scripta Materialia*, 2012, **66**, 1049-1052.
2. R. Raj, M. Cologna and S. C. Francis John, *Journal of the American Ceramic Society*, 2011, **94**, 1941-1965.
3. R. I. Todd, E. Zapata-Solvas, R. S. Bonilla, T. Sneddon and P. R. Wilshaw, *Journal of the European Ceramic Society*, 2015, **35**, 1865-1877.
4. B. Reeja-Jayan, K. L. Harrison, K. Yang, C.-L. Wang, A. E. Yilmaz and A. Manthiram, *Sci. Rep.*, 2012, **2**, 1003.
5. N. Nakamura, M. Terban, S. J. L. Billinge and B. Reeja-Jayan, *Journal of Materials Chemistry A*, 2017, **5**, 18434-18441.
6. M. A. E. Diwiny, E. Hassanen, A. M. El-Sayed and G. Abouelmagd, 2014.
7. 2000.
8. M. Rees, *Journal*, 2018.
9. S. K. Jha, X. L. Phuah, J. Luo, C. P. Grigoropoulos, H. Wang, E. García and B. Reeja-Jayan, *Journal of the American Ceramic Society*, 2018, **0**.
10. T. Egami and S. J. L. Billinge, *Underneath the Bragg Peaks: Structural Analysis of Complex Materials*, Elsevier, 2012.
11. C. L. Farrow, P. Juhas, J. W. Liu, D. Bryndin, E. S. Božin, J. Bloch, T. Proffen and S. J. L. Billinge, *J. Phys. Condens. Matter*, 2007, **19**, 335219.
12. N. Nakamura, J. Seepaul, J. B. Kadane and B. Reeja-Jayan, *Appl. Stochastic Models Bus. Ind.*, 2017.
13. H. Xue, X. Kong, Z. Liu, C. Liu, J. Zhou, W. Chen, S. Ruan and Q. Xu, *Appl. Phys. Lett.*, 2007, **90**, 201118.
14. C. O. Kappe, *Chem. Soc. Rev.*, 2013, **42**, 4977-4990.
15. U. Diebold, *Surface Science Reports*, 2003, **48**, 53-229.
16. D. A. H. Hanaor and C. C. Sorrell, *J. Mater. Sci.*, 2011, **46**, 855-874.
17. P. Bouvier, E. Djurado, G. Lucazeau and T. Le Bihan, *Physical Review B*, 2000, **62**, 8731-8737.
18. S. Fabris, A. T. Paxton and M. W. Finnis, *Acta Mater.*, 2002, **50**, 5171-5178.
19. F. Zhang, P. J. Chupas, S. L. A. Lui, J. C. Hanson, W. A. Caliebe, P. L. Lee and S.-W. Chan, *Chem. Mater.*, 2007, **19**, 3118-3126.
20. P. Bouvier, E. Djurado, G. Lucazeau and T. Le Bihan, *Phys. Rev. B*, 2000, **62**, 8731-8737.
21. N. Nakamura and B. Reeja-Jayan, *Journal of Materials Research*, 2019, **34**, 194-205.
22. S. K. Jha, N. Nakamura, S. Zhang, L. Su, P. M. Smith, X. L. Phuah, H. Wang, H. Wang, J. S. Okasinski, A. J. H. McGaughey and B. Reeja-Jayan, *Adv. Eng. Mater.*, 2019, **21**, 1900762.
23. B. Gutmann, D. Obermayer, B. Reichart, B. Prekodravac, M. Irfan, J. M. Kremsner and C. O. Kappe, *Chem. Eur.*, 2010, **16**, 12182-12194.
24. J. Jeong, N. Aetukuri, T. Graf, T. D. Schladt, M. G. Samant and S. S. P. Parkin, *Science*, 2013, **339**, 1402.
25. N. Lu, P. Zhang, Q. Zhang, R. Qiao, Q. He, H.-B. Li, Y. Wang, J. Guo, D. Zhang, Z. Duan, Z. Li, M. Wang, S. Yang, M. Yan, E. Arenholz, S. Zhou, W. Yang, L. Gu, C.-W. Nan, J. Wu, Y. Tokura and P. Yu, *Nature*, 2017, **546**, 124.

26. T. B. Holland, U. Anselmi-Tamburini, D. V. Quach, T. B. Tran and A. K. Mukherjee, *J. Eur. Ceram.*, 2012, **32**, 3659-3666.
27. K. M. Ø. Jensen, M. Christensen, P. Juhas, C. Tyrsted, E. D. Bøjesen, N. Lock, S. J. L. Billinge and B. B. Iversen, *J. Am. Chem. Soc.*, 2012, **134**, 6785-6792.
28. M. J. Taylor and J. M. Coddington, *Polyhedron*, 1992, **11**, 1531-1544.
29. P. Juhás, D. M. Cherba, P. M. Duxbury, W. F. Punch and S. J. L. Billinge, *Nature*, 2006, **440**, 655-658.
30. D. Prill, P. Juhas, M. U. Schmidt and S. J. L. Billinge, *J. Appl. Crystallogr.*, 2015, **48**, 171-178.
31. T. Egami and S. J. L. Billinge, *Underneath the Bragg Peaks: Structural Analysis of Complex Materials*, Elsevier, 2012.
32. I. K. Jeong, T. Proffen, F. Mohiuddin-Jacobs and S. J. L. Billinge, *J. Phys. Chem. A*, 1999, **103**, 921-924.
33. K. Kodama, S. Iikubo, T. Taguchi and S. Shamoto, *Acta Cryst.*, 2006, **A62**, 444-453.
34. E. A. Meulenkamp, *J. Phys. Chem. B*, 1998, **102**, 5566-5572.
35. L. Gamez-Mendoza, M. W. Terban, S. J. L. Billinge and M. Martinez-Inesta, *J. Appl. Cryst.*, 2017, **50**, 741-748.
36. C. Tyrsted, K. M. Ø. Jensen, E. D. Bøjesen, N. Lock, M. Christensen, S. J. L. Billinge and B. Brummerstedt Iversen, *Angew. Chem. Int. Ed.*, 2012, **51**, 9030-9033.
37. C. K. Christensen, E. D. Bøjesen, D. R. Sørensen, J. H. Kristensen, J. K. Mathiesen, B. B. Iversen and D. B. Ravnsbæk, *ACS Appl. Nano Mater.*, 2018, **1**, 5071-5082.
38. A. A. Bolzan, C. Fong, B. J. Kennedy and C. J. Howard, *Acta Cryst. B*, 1997, **53**, 373-380.
39. F. Lawson, *Nature*, 1967, **215**, 955-956.
40. J. Köhler, J. Tong, R. Dinnebier and A. Simon, *Z. anorg. allg. Chem.*, 2012, **638**, 1970-1975.
41. B. Eifert, M. Becker, C. T. Reindl, M. Giar, L. Zheng, A. Polity, Y. He, C. Heiliger and P. J. Klar, *Phy. Revi. Mater.*, 2017, **1**, 014602.
42. A. Seko, A. Togo, F. Oba and I. Tanaka, *Phys. Rev. Lett.*, 2008, **100**, 045702.
43. H. Peng, *Phys. Lett. A*, 2008, **372**, 1527-1530.
44. F. Wang, C. Di Valentin and G. Pacchioni, *Phy. Rev. B*, 2011, **84**, 073103.
45. Z. M. Jarzebski and J. P. Marton, *J. Electrochem. Soc.*, 1976, **123**, 199C.
46. A. Bouzoubaa, A. Markovits, M. Calatayud and C. Minot, *Surf. Sci.*, 2005, **583**, 107-117.
47. K. G. Godinho, A. Walsh and G. W. Watson, *J. Phys. Chem. C*, 2009, **113**, 439-448.
48. G. Pacchioni, *ChemPhysChem*, 2003, **4**, 1041-1047.
49. R. D. Shannon and J. A. Pask, *J. Am. Ceram. Soc.*, 1965, **48**, 391-398.
50. B. Choudhury and A. Choudhury, *Int. Nano Lett.*, 2013, **3**, 55.
51. E. U. Donev, J. I. Ziegler, R. F. Haglund Jr and L. C. Feldman, *J. Opt.*, 2009, **11**, 125002.
52. S. K. Jha, H. Charalambous, H. Wang, X. L. Phuah, C. Mead, J. Okasinski, H. Wang and T. Tsakalakos, *Ceram. Int.*, 2018, **44**, 15362-15369.
53. S. K. Jha, X. L. Phuah, J. Luo, C. P. Grigoropoulos, H. Wang, E. García and B. Reeja-Jayan, *J. Am. Ceram. Soc.*, 2019, **102**, 5-31.
54. J. M. Lebrun, C. S. Hellberg, S. K. Jha, W. M. Kriven, A. Steveson, K. C. Seymour, N. Bernstein, S. C. Erwin and R. Raj, *J. Am. Ceram. Soc.*, 2017, **100**, 4965-4970.
55. B. Yoon, D. Yadav, R. Raj, E. P. Sortino, S. Ghose, P. Sarin and D. Shoemaker, *J. Am. Ceram. Soc.*, 2018, **101**, 1811-1817.
56. B. Gilbert, F. Huang, H. Zhang, G. A. Waychunas and J. F. Banfield, *Science*, 2004, **305**, 651.
57. V. V. T. Doan-Nguyen, S. A. J. Kimber, D. Pontoni, D. Reifsnyder Hickey, B. T. Diroll, X. Yang, M. Miglierini, C. B. Murray and S. J. L. Billinge, *ACS Nano*, 2014, **8**, 6163-6170.

58. T. L. Christiansen, E. D. Bøjesen, M. Juelsholt, J. Etheridge and K. M. Ø. Jensen, *ACS Nano*, 2019, **13**, 8725-8735.
59. A. S. Masadeh, E. S. Božin, C. L. Farrow, G. Paglia, P. Juhas, S. J. L. Billinge, A. Karkamkar and M. G. Kanatzidis, *Phys. Rev. B*, 2007, **76**, 115413.
60. C. R. A. Catlow, K. M. Diller and M. J. Norgett, *J. Phys. C: Solid State Phys.*, 1977, **10**, 1395-1412.
61. G. V. Lewis and C. R. A. Catlow, *J. Phys. C: Solid State Phys.*, 1985, **18**, 1149-1161.
62. M. Youssef, K. J. Van Vliet and B. Yildiz, *Phys. Rev. Lett.*, 2017, **119**, 126002.
63. R. D. Shannon, *Journal of Applied Physics*, 1993, **73**, 348-366.
64. M. R. Telmer, M. S. Hilario, B. W. Hoff, M. T. Lanagan and B. Reeja-Jayan, *Journal of Physics: Condensed Matter*, 2019, **31**, 225702.
65. K. C. Kao, *Dielectric Phenomena in Solids*, Elsevier: Academic Press, 2004.
66. E. Saenz, L. Rolo, K. van't Klooster, M. Paquay and V. V. Parshin, *Proceedings of 6th European Conference on Antennas and Propagation, EuCAP*, 2012, 572-576.
67. G. J. Simonis and R. D. Felock, *Applied Optics*, 1983, **22**, 194-198.
68. S. Kasap and P. Capper, *Springer Handbook of Electronic and Photonic Materials.*, Springer, 2017.
69. R. Summitt, *Journal of Physics D: Applied Physics*, 1968, **39**, 3762-3767.
70. A. Boonchun and W. R. L. Lambrecht, *Physical Review B*, 2010, **81**, 235214.
71. R. D. Shannon, *Journal of Physics D: Applied Physics*, 1992, **73**, 348-366.
72. R. C. Marshall and J. A. Adamski, *Defense Technical Information Center*, 1979, 1-26.
73. S. Botti, N. Vast, L. Reining, V. Olevano and L. C. Andreani, *Physical Review Letters*, 2002, **89**, 216803:216801-216804.
74. V. Randle and O. Engler, *Introduction to Texture Analysis: Macrotexture, Microtexture and Orientation Mapping*, CRC Press, 2000.
75. W. Ludwig, S. Schmidt, E. M. Lauridsen and H. F. Poulsen, *Journal of Applied Crystallography*, 2008, **41**, 302-309.
76. A. F. Arif, R. Balgis, T. Ogi, F. Iskandar, A. Kinoshita, K. Nakamura and K. Okuyama, *Scientific Reports*, 2017, **7**, 3646.